Discrete ply modelling of aeronautical intermediate-scale notched carbon fibre reinforced thermoplastic specimens subjected to multiaxial loading

José Guerrero, Christophe Bouvet, John-Eric Dufour, Joël Serra

To cite this version:

José Guerrero, Christophe Bouvet, John-Eric Dufour, Joël Serra. Discrete ply modelling of aeronautical intermediate-scale notched carbon fibre reinforced thermoplastic specimens subjected to multiaxial loading. Composite Structures, 2025, 361, pp.119042. ⟨10.1016/j.compstruct.2025.119042⟩. ⟨hal-05175948⟩

HAL Id: hal-05175948
https://hal.science/hal-05175948v1

Submitted on 22 Jul 2025

Discrete ply modelling of aeronautical intermediate-scale notched carbon fibre reinforced thermoplastic specimens subjected to multiaxial loading

José M. Guerrero[a,*], Christophe Bouvet[b], John-Eric Dufour[b], Joël Serra[b]

[a]AMADE, Polytechnic School, Universitat de Girona, Campus Montilivi s/n, E-17003 Girona, Spain
[b]Institut Clément Ader (UMR 5312), ISAE-SUPAERO – INSA – IMT Mines Albi – UPS – CNRS, Toulouse, France

---

Abstract

Several finite element models developed at the mesoscale level are available for predicting the strength and failure progression of composite materials. However, this kind of damage models are commonly validated by comparing with typical coupon-scale testing specimens under uniaxial loading, which are not fully representative of aeronautical structures subjected to complex multiaxial loads. In this work, the Discrete Ply Model (DPM) is employed to reproduce intermediate-scale experimental tests carried out on carbon fibre reinforced thermoplastic samples, with a sharp central notch of 100 mm, tested in the VERTEX rig under tension, shear, and combined tension and shear loading. The tests show early buckling (particularly for the shear and combined cases) and development of post-buckling for almost the entire loading. The numerical results obtained demonstrate that the strengths, the fluxes as a function of the applied strains, deformed shapes, buckling modes, crack propagations and failure patterns are predicted with reasonable accuracy.

Keywords: Thermoplastic, Finite element analysis (FEA), Multiaxial loading, Structural scale specimens

---

1. Introduction

Carbon Fibre Reinforced Polymer (CFRP) composites are nowadays widely used for lightweight applications, such as in aerospace, wind turbines, automotive, etc., thanks to their excellent stiffness and strength to weight ratio [1–3]. Nonetheless, one major drawback of CFRP is their inherent brittle and complex failure behaviour, which involves several failure mechanisms that occur altogether, such as fibre breakage, kinking and pull-out, matrix cracking, delamination and fibre-matrix debonding.

The development and certification of composite structures is still based on the so-called Building Block Approach (BBA) [3–8], which consists in a pyramid of levels, going from coupon size up to full-scale tests. At the lowest level of the pyramid, tests are carried out on coupons under uniaxial loading, allowing to characterise the materials and obtain design allowables [3, 9]. Testing becomes more complex for the higher levels of the pyramid, where structural details are tested, until the highest level, where the full component is tested. However, these tests are commonly limited to uniaxial loading [3].

---

[*] Corresponding author. Tel.: +34 972 41 88 17.
Email address: `josemanuel.guerrero@udg.edu` (José M. Guerrero)

Composite structures are assembled by bolts, therefore, the presence of holes or cut-outs, which lead to complex stress concentration and a strength reduction, is unavoidable [6, 10]. Commonly, the strength reduction of holes is determined by carrying out open hole tests, at the lowest levels of the pyramid [10–14]. Nonetheless, open hole tests are limited to small coupons under uniaxial loading and thus, may not be representative of composite structures subjected to complex multiaxial loading. Moreover, open hole specimens commonly fail catastrophically, while in a larger structure, the crack propagates more progressively [10]. This is an important fact, since aircraft manufacturers must certify their structure is safe under static loads with a large crack that could occur due to an exceptional event [6].

In order to accurately design CFRP components, it is relevant to test specimens that are representative of the real counterparts, and under complex loading, similar to the loads encountered for instance in an aircraft under service. There are few testing rigs in the world that are able to test structural elements (i.e. specimens at the middle level or at the top of the pyramid) under complex loading [3, 10]. Basically two types of these machines exist. In the first type, loading is applied to the specimen directly from the actuators, with the downside that many actuators are needed to generate compression or shear. In the second type of machine, the specimen is part of a larger structure (usually with a box shape), which is loaded by actuators [3, 15, 16]. This allows to generate combined tension/bending/torsion loading, which is more representative of the multiaxial loading found in aeronautical parts when in service. The drawback of these tests is that evaluating the forces supported by the specimen is more difficult than in traditional universal testing machines.

Almost uniquely in the world, the VERTEX testing rig of the Institut Clément Ader (Toulouse, France) is one of the few machines able to test large composite specimens (at the intermediate scale of the test pyramid). Hence, the machine is capable of testing, for instance, specimens representative of fuselage sections under multiaxial loading, at moderate cost. The details and validation of this rig were presented in Serra *et al.* [3, 6]. Recently, Grotto *et al.* [10] used the VERTEX machine for testing thin flat CFRP thermoplastic specimens (558 x 536 mm^2) with a large, sharp central notch of 100 mm, under combined loadings of tension, shear and internal pressure. The results showed that pressure led to an earlier failure initiation for shear tests, but not for tension. Shear loading always led to earlier failure, regardless of the presence of combined pressure or not. These results therefore allow to get a more representative overview of the presence of a large notch, than the traditional open hole test.

Due to the large amount of experimental tests required to certify composite structures, and the complexity involved in testing composite parts under combined loading, the literature is continuously working towards developing numerical models with enough predictive capabilities, able to replace real experimental tests [7]. Nowadays, several models are available in the literature developed at different scales: macromechanical models [17, 18], mesomechanical models [8, 12, 19–25], and micromechanical [26–29]. Macromechanical models assume an homogeneous material, meaning that the interaction between plies cannot be captured and thus, they are severely limited. On the other extreme, micromechanical models physically take into account the presence of the fibre and matrix and their interaction, being more realistic.

Unfortunately, prohibitive computational requirements are needed to simulate even small specimens. For this reason, mesomechanical models stand as the best compromise, since these can capture delamination, while fibre breakage and matrix cracking can be modelled by means of intraply damage variables.

Mesomechanical models can be categorised according to their level of discretisation [12]: from models fully based on continuum damage mechanics (without including cohesive interfaces), to models fully discretised (including interface elements to capture fibre breakage, delamination and matrix cracking). For example, Maimí *et al.* [19, 20] developed a continuum damage model able to capture the damage onset and evolution of composite materials. A more advanced 3D version of this approach, including plasticity, was recently presented by Cózar *et al.* [24, 25]. These models are fully continuum, excluding the use of interface elements. Chen *et al.* [13] proposed a smeared crack model, which used continuum mechanics to model fibre and matrix failure, combined with cohesive interfaces to capture delamination. Bouvet *et al.* [30] originally developed the Discrete Ply Model (DPM), which was refined in subsequent studies [12]. In this approach, solid elements (including a damage variable) are used to capture fibre breakage, while interface elements are employed to capture matrix cracking and delamination.

With the objective of simulating damage progression, but with lower computational efforts, other approaches such as the Equivalent Single-Layer (ESL) or the Layer-Wise (LW) have also been developed [31, 32]. ESL models assume uniform kinematics through all the thickness, with the stiffness matrix of each layer being homogenised. In contrast, LW models take into account different sets of variables for each layer, with a displacement continuity being imposed at the layer interfaces. With this context, Trombini *et al.* [32] recently presented a Hashin-based orthotropic damage model, linked with higher-order one-dimensional elements, capable of capturing both the ultimate load and the crack propagation.

Nowadays, current available numerical models have been well proven under different loading conditions and have been employed to reproduce different tests at the lower levels of the pyramid. However, to the authors' best knowledge, few studies exist presenting damage simulations performed at the higher levels of the pyramid, especially, under multiaxial loading. For example, Serra *et al.* [33] used the DPM to reproduce experiments on large notched coupons, although these were limited to pure tension tests. Later, Serra *et al.* [34] used again the DPM to simulate medium velocity impacts and complex loadings after impact on large composite panels. Good correlation between the DPM and experiments were found.

As a follow up from previous research [3, 6, 10, 12, 33], in this work the DPM is employed to reproduce intermediate-scale experimental tests on thermoplastic carbon notched samples tested in the VERTEX rig under combined loading. While previous work already showed the capabilities of the DPM to reproduce experiments on large notched coupons [33, 34], simulations were limited to pure tensile tests [33], and to unnotched panels [34] and thus, this paper goes one step forward. The aim and originality of the study is to demonstrate the capabilities of the numerical model to capture the failure mechanisms of notched specimens of higher levels of the pyramid of tests under multiaxial loading. Moreover, the model attempts to reproduce not only the strength found in these tests, but also the crack propagation (failure pattern) and the deformed shape. Another highlight of this work is that the tests show early buckling and development of post-buckling during almost the entire tests. The results obtained show that shear, tension and combined tests were successfully reproduced in terms of strength and failure pattern, proving that accurate virtual testing is not only limited to the lower levels of the pyramid, and that the DPM approach is robust. The paper is organised as follows. First, a summary of the experimental testing campaign and the finite element approach are described. After that, the results and discussion are presented for the three cases analysed and eventually, some conclusions are drawn. All the data shown in this study is normalised due to confidentiality. It is worth noting that this paper will focus on the numerical side (i.e. to reproduce the experiments), rather than analysing the experimental results, since this was performed in another paper [10].

2. Materials and methods

This section presents the materials, experimental testing campaign and the finite element models that were developed in this work.

2.1. Experimental campaign

The experimental testing campaign was carried out by using the VERTEX testing machine of the Institute Clement Ader (Toulouse, France), which is able to perform multiaxial tests [3, 6]. The same specimens presented and analysed in Grotto *et al.* [10] are here considered again. The specimen consists on a 558×536 mm^2 planar plate with 128 holes, that are used to bolt the specimen to the VERTEX machine. Thus, the actual 'free area' of the specimen during testing is about 400×400 mm^2. The stacking sequence cannot be revealed due to confidentiality, but we note that the specimens are quasi-isotropic, with the same number of plies oriented at 0°, 90°, +45° and -45°. The material consists in an aeronautical thermoplastic carbon fibre reinforced polymer, with a total of 8 plies. The specimens have a centre-notch 100 mm long with an end notch radius of 1 mm, see Fig. 1.

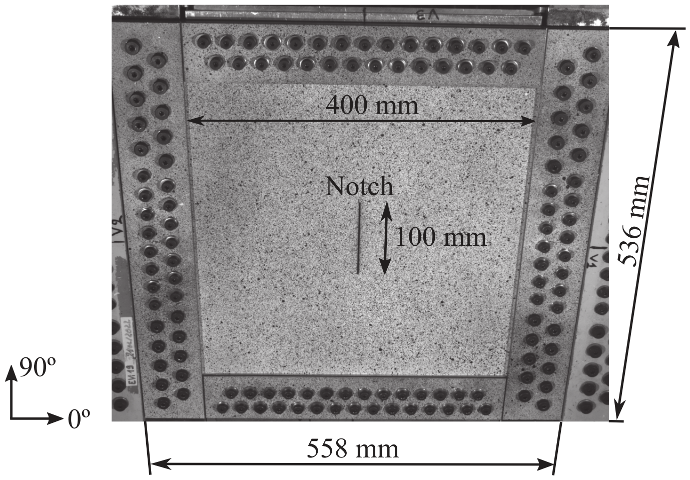

Figure 1: Geometry and dimensions of the notched specimens tested in the VERTEX machine.

To manufacture the plates, the consecutive plies were stacked on to another and held together by pressing a soldering iron on the current top ply [10]. The material was then cured at high pressure and temperature (above 300 ºC) following the manufacturer's guidelines. For more details of the manufacturing process, the reader is referred to [10].

As stated, the VERTEX test rig is used to carry out the experimental campaign, see Fig. 2. The test bench consists in a tubular box with four actuators. The specimen is bolted at the central part and in the upper face. The four jacks are used to obtain the desired loading conditions. Jacks 1 and 2 (see Fig. 2a) push or pull symmetrically the box, causing it to bend. Thus, with these conditions, the specimen is subjected to either tension or compression (Fig. 2c). On the other hand, jacks 3 and 4 generate torsional loading in the central box, and thus, loading the specimen in shear (Fig. 2c). In addition, an air-pressurised rubber bladder can be included in the central box to subject the specimen under pressure, although this was not performed in this paper. The four jacks can be controlled independently to obtain any loading combination: tension/compression + shear + pressure. In total, three different tests are considered in this study: a) tension, b) shear and c) combined tension and shear. After bolting the specimens to the bench, loading was slowly applied until the crack propagation was significantly long and the specimen failed. Two specimens were tested for each case. In addition to this, two optical cameras are located on top of the specimen, which are used for performing Digital Image Correlation (DIC), while an infrared camera is employed to detect and follow the crack length, see Fig. 2b.

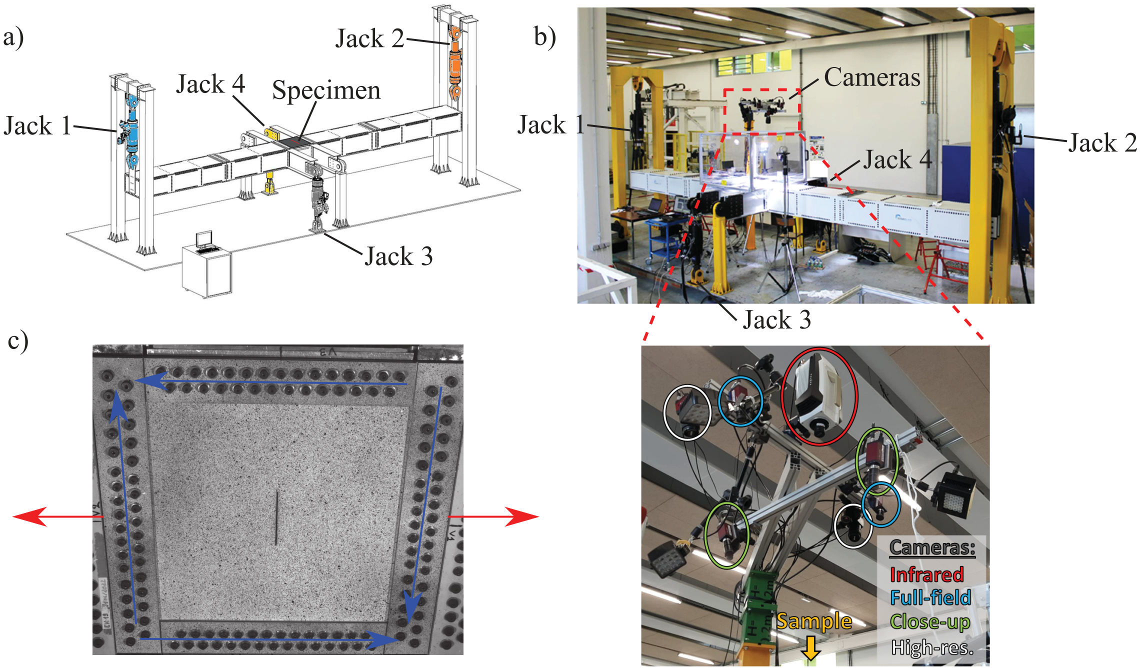

Figure 2: VERTEX testing rig. a) Scheme of the VERTEX machine, b) photo of the real machine, including also the cameras for monitoring, and c) representation of the loading conditions obtained in the specimen.

To perform DIC, a random black speckle pattern was painted at the outer surface of the free region of the specimen (about 400 × 400 mm^2 of area), and pictures were taken by using the full-field optical cameras with a frequency of 2 frames per second. The commercial software VIC-3D 7, with a local subset method (subset=29 px, step=7 px, filter=15 px, 1 px = 0.28 mm) [10], was used to obtain the displacements based on the pictures.

Due to the complexity of the VERTEX bench, a classical load-displacement or stress-strain curve cannot be obtained for the tests. Therefore, the same approach carried out previously [10] is employed to obtain fluxes and strains representative of the loading conditions from the DIC data. Fluxes are computed based on the calculation of the first and second derivatives of the out-of-plane and in-plane displacement, using classical laminate theory, with a 5 mm step between neighbour point values. For each frame available during the test, the longitudinal flux (N_{xx}) is computed as the average value contained in the boxes illustrated in Fig. 3a, while the shear flux (N_{xy}) is obtained as the average of the four boxes defined in Fig. 3b. Notice that the boxes are located close to the borders of the specimen and far away from the notch, so that these can be representative of the loading of the specimen. In addition, for the tensile test, only the flux N_{xx} has a significant value (since this corresponds with the applied load), while the shear test mainly has N_{xy} flux. The combined shear plus tension case has a significant amount of both fluxes. Moment fluxes were not analysed since these can be neglected for these tests [10]. Moreover, the DIC data was also employed to compute global strains. The longitudinal global strain, $\varepsilon_{\mathrm{xx}}$, is computed as

$$\varepsilon_{\mathrm{xx}} = \frac{U_{\mathrm{R}} - U_{\mathrm{L}}}{X_{\mathrm{R}} - X_{\mathrm{L}}} \tag{1}$$

where U_{R} and U_{L} are the average longitudinal displacements (x direction) of the right and left boxes, respectively, while $X_{\mathrm{R}} - X_{\mathrm{L}}$ is the horizontal distance between both boxes in mm, see Fig. 3a. Likewise, the global shear strain, $\varepsilon_{\mathrm{xy}}$, is computed as

$$\varepsilon_{\mathrm{xy}} = \frac{U_{\mathrm{T}} - U_{\mathrm{B}}}{2(Y_{\mathrm{T}} - Y_{\mathrm{B}})} + \frac{V_{\mathrm{R}} - V_{\mathrm{L}}}{2(X_{\mathrm{R}} - X_{\mathrm{L}})} \tag{2}$$

where V_{R} and V_{L} are the average transverse displacements (y direction) of the right and left boxes, respectively, U_{T} and U_{B} are the average longitudinal displacements (x direction) of the top and bottom boxes, respectively, while $Y_{\mathrm{T}} - Y_{\mathrm{B}}$ is the vertical distance between both boxes in mm, see Fig. 3b. Therefore, for the tensile test, the $N_{\mathrm{xx}} - \varepsilon_{\mathrm{xx}}$ curve is obtained, while for the shear and the combined test, both $N_{\mathrm{xx}} - \varepsilon_{\mathrm{xx}}$ and $N_{\mathrm{xy}} - \varepsilon_{\mathrm{xy}}$ curves are analysed as explained later.

The infrared cameras are used to monitor and obtain the crack length along the test. The cameras were set up to monitor a window of 320×256 px^2 with a frequency of 100 FPS, which is a low resolution, but enough to detect failure signals and follow the crack with detail. As a consequence of the different thermal emissivity and local surface orientations, all the involved components (sample, tabs, notch, bolts, etc.) can be fully distinguished. During testing, a local increase in temperature of 1ºC indicates fibre failure [33]. Other failure modes, such as matrix cracking or delamination, produce much smaller thermal increase (few tenths of a degree) and are more difficult to observe. Hence, the infrared measurement allows to detect fibre breakage through the entire specimen thickness, something that is not possible with DIC. During the test, as the crack starts to propagate, heat dissipation becomes clearly visible, which allows to locate the crack tip and even to see the shape of the crack. As in previous work [10, 35], the crack front is assumed to be located at the centre of the heat spot, since the width of the spot is attributed to heat diffusion and not to diffused damage [35]. Therefore, the crack length is computed as the distance between the centre of the

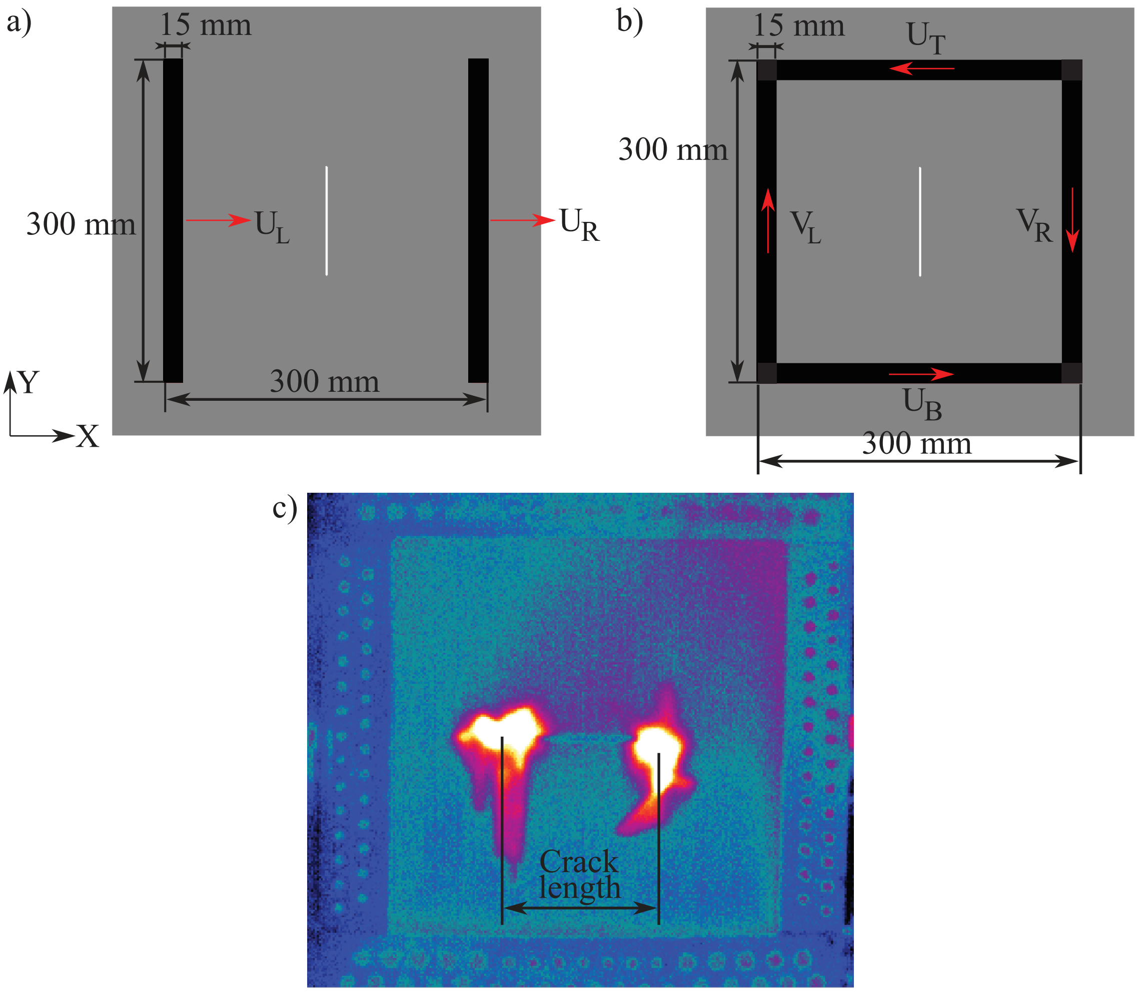

Figure 3: Post-processing of the experimental results. a) Definition of boxes to obtain the longitudinal flux and strain, b) boxes used to compute the shear flux and strain and c) infrared frame showing the approach to compute the crack length.

heat at the two sides of the notch, see Fig. 3c.

2.2. Finite element model

This section presents the Finite Element (FE) model that was developed for reproducing the experimental campaign presented in Section 2.1, carried out in the multiaxial VERTEX test bench (Fig. 2).

The commercial finite element software Abaqus/explicit 2018 [36] has been employed to carry out the simulations. In total, three different models have been developed to reproduce the following tests: a) tension, b) shear and c) combined tension and shear. The model is identical for the three cases, with only the boundary conditions being different accordingly to the desired loading conditions. In order to model the progressive failure of the composite material, the Discrete Ply Model (DPM) approach has been employed [12, 30, 37]. While this method has been greatly described elsewhere [12, 30, 37], the basics of the methodology are here briefly presented for the reader's convenience.

Fig. 4 shows a schematic representation of the DPM approach. The DPM is able to predict the three main failure mechanisms that occur in composites: intra-ply fibre failure, intra-ply matrix cracking and inter-ply delamination. One of the main innovative concepts of the DPM is the use of a specific mesh set up, consisting in a combination of 3D solid elements and zero-thickness interface (cohesive) elements. The objective of the 3D volume elements is to capture fibre breakage, while the interface elements are meant to capture matrix cracking and delamination. The mesh is oriented with the fibre orientation, which allows to capture accurately matrix cracking. Therefore, the mesh set up has 4 nodes at each point (see Fig. 4). In this way, 2 of them allow to model the matrix cracking of the upper ply; the 2 others allow to capture the matrix cracking of the lower ply and the 2 pairs of nodes are linked together by delamination elements. Thus, a natural coupling between delamination and matrix cracking is established. The downside of this approach is that it requires a complex mesh (with coincident nodes) at the interfaces between the cohesive elements and the 3D elements. In addition, the use of an oriented mesh increases even more the complexity for creating it. Unfortunately, the generation of such mesh is too complex to be generated in Abaqus directly. For this reason, an in-house Fortran routine is used to generate the desired mesh, which is afterwards imported into Abaqus. Notice that one element through-the-thickness of each ply is used.

Compared with traditional standard models, e.g. Abaqus built-in Hashin damage model, the DPM is fully 3D, not being limited to plane stress elements, such as shell or continuum shell elements, as the Hashin model available in Abaqus. Moreover, splitting and delamination are more accurately captured thanks to the specific mesh set up.

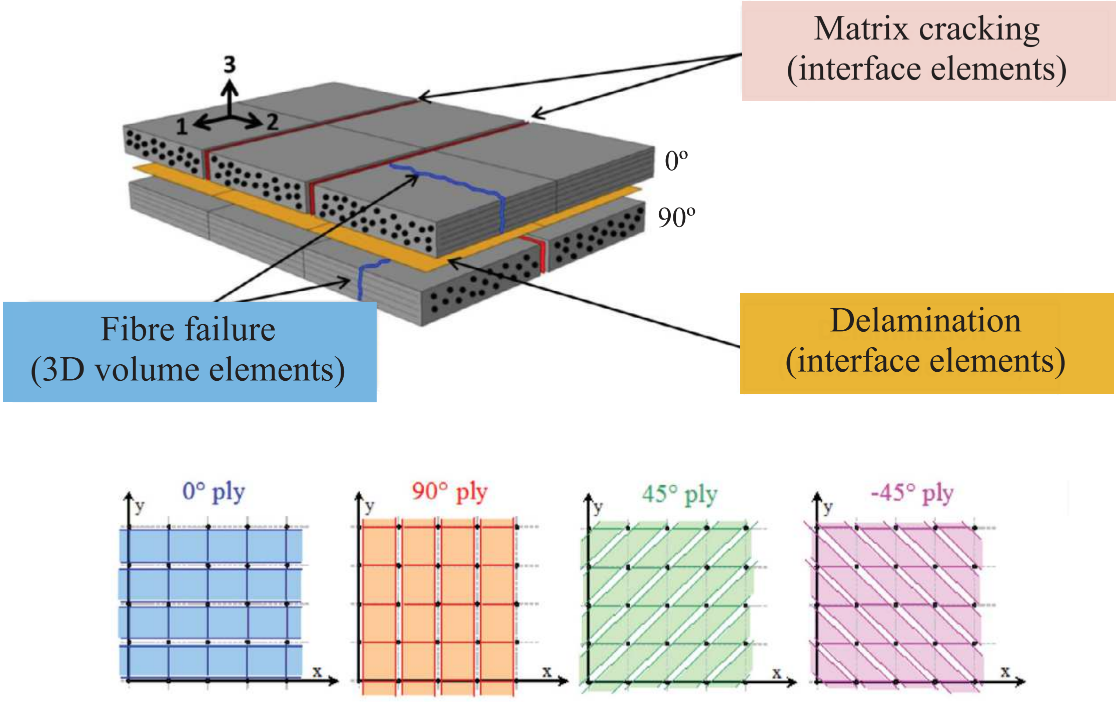

Figure 4: Schematic representation of the discrete ply model approach, showing the different type of elements, interfaces used and mesh set up [6].

Fibre breakage is accounted for by the volume elements (Fig. 4). In order to model the progressive failure, a continuum damage mechanics approach is used. Thus, longitudinal failure is initiated when the strain in the fibre direction reaches the longitudinal failure strain of the ply. Then, the stiffness of the volume element is gradually reduced until the critical fracture toughness has been dissipated, essentially following a linear softening law. Abaqus C3D8 elements were used (an eight node, 3D linear element with full integration), in order to have an accurate bending behaviour with only one element through the ply thickness. To ensure that the correct amount of energy is dissipated for each element, a communication law between the 8 integration points is used. Mesh independence is ensured by regularising the dissipated energy with respect to the characteristic element length, so that constant energy is released per unit area independently of the element length.

Matrix cracking is captured by means of the interface elements normal to the transversal direction (Fig. 4). Hashin failure criterion [38] is evaluated in the neighbouring volume elements. If the Hashin matrix failure criterion is met in either of the neighbouring solid elements failure is assumed to occur. Then, a classical linear cohesive law is used in order to degrade the penalty stiffness of the interface element according to the corresponding critical fracture toughness. Once all energy is dissipated, the penalty stiffness of the interface (initially 10^6 MPa/mm) is set equal to zero to simulate the generation of a transverse crack.

Similar to matrix cracking, delamination is modelled using the cohesive element interfaces between two consecutive plies of different orientation (Fig. 4). Damage of the delamination elements is driven by a classical linear cohesive law that depends on the mode I and mode II strengths as well as the fracture toughnesses. Linear softening is employed. The DPM is implemented by using a vumat subroutine in Abaqus/explicit. In total, the model only needs 13 material properties: 5 elastic constants, transverse and shear strengths, tensile and compressive longitudinal failure strains, the longitudinal fracture toughness in tension and compression, and the mode I and mode II fracture toughnesses. All properties were measured by following the appropriate test standards [39–44], except for the longitudinal tensile fracture toughness, which was adjusted numerically. The material properties values used cannot be revealed due to confidentiality. For further details of the DPM, the reader is referred to [12, 30, 37].

Fig. 5 presents a picture of the full FE model geometry including also the mesh. All the dimensions match the experimental ones. The stacking sequence cannot be revealed due to confidentiality. The specimens have a centre notch of 1 mm radius and 100 mm length, see Fig. 5. Modelling the entire specimen dimensions using the DPM approach would lead to millions of elements and a prohibitive computational time. Therefore, the specimen plate was split up into two regions. The first region, of dimensions 200×60 mm^2, includes the notch and is modelled with the DPM (i.e., it contains 3D solid elements and interface elements). The in-plane mesh size used in this region is about twice the ply thickness for the volume and interface elements. This dimension is motivated by the fact that experimental observations show that, commonly, two matrix cracks are separated by a distance ranging from 1.5 to 2 times the ply thickness [45]. The validity of using this mesh size was also explored in Serra *et al.* [12]. In addition, all plies are modelled with one element per ply thickness, as it is commonly done in the literature. The use of fully integrated elements allows to capture well the stress through-the-thickness of the plies with a single element.

The remaining of the plate, corresponding to region 2, contains Abaqus continuum shell elements SC8R

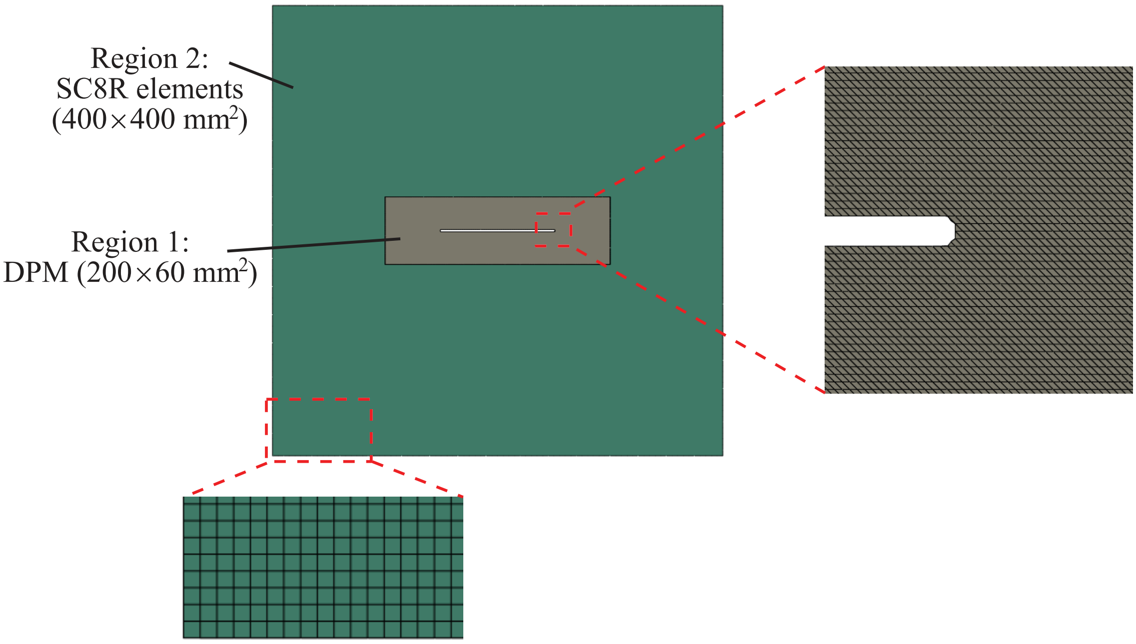

Figure 5: Full FE model of the tested specimens, with the two regions used for modelling and a zoomed view of the mesh in both regions.

(eight node continuum shell elements with reduced integration). These kind of elements have displacement degrees of freedom like solid elements, but their kinematic formulation is similar to that of shell elements [36]. In this region, a coarse mesh size of 5 mm is used, together with a single element through the entire laminate thickness. The composite layup feature of Abaqus, which is based on classical laminate theory, is used to account for the stacking sequence in this region. In this area no damage is modelled, being elastic for the entire simulation. Thanks to this approach, we model damage where it is needed (close to the notch) while far from it, the computational requirements are reduced by using the SC8R elements. Tie constraints are employed to merge both regions. In total, the models have 1091064 elements and 1545480 nodes.

Due to the complex loading imposed by the VERTEX test rig, especially in the shear and in the combined (tension plus shear) cases, boundary conditions well representative of the tests have to be imposed in the FE model. To do so, DIC was used in the experimental campaign to obtain the displacement fields during the tests (see Section 2.1 for all details). These fields are imposed in the model as displacement boundary conditions, allowing to faithfully apply the same loading conditions as occurred in the real tests. To properly do this, the same strategy used in previous work [3, 6] was employed. Four squares of nodes are selected where the displacements are imposed, see Fig. 6. The three displacement components (x, y and z), obtained by DIC, are imposed on the outer nodes, forming a 300×300 mm^2 square, see Fig. 6. Then, in order to be able to capture well the rotations, an out-of-plane displacement (Uz) is imposed on the remaining inner 3 rows of nodes (Fig. 6). The boundary conditions are imposed node by node, and degree of freedom by degree of freedom. Notice that the only difference between the three models (tension, shear and combined tension plus shear), is the displacement values applied in these nodes. It is worth mentioning that before starting the test, some pretension is applied into the specimen due to the bolts that are used to screw the specimen into the vertex test rig (Fig. 1). The effect of the pretension in the model is also accounted for since the DIC displacements were started to be recorded before bolting the specimen.

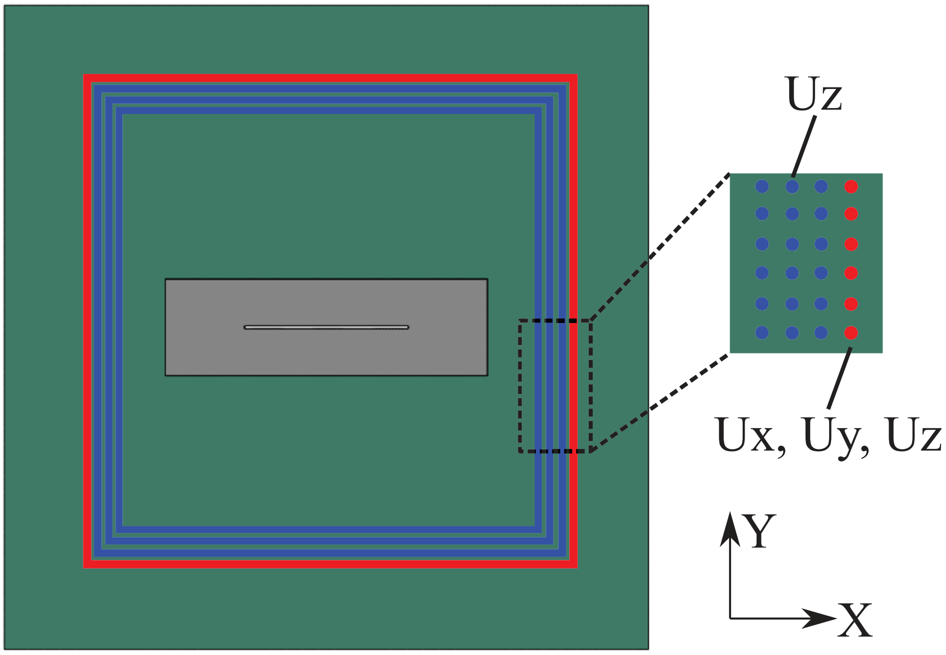

Figure 6: Boundary conditions applied into the FE model extracted from DIC. All displacements are imposed in the outer nodes (in red), and only the out-of-plane displacement to the inner nodes (coloured blue).

Explicit time integration was used to avoid convergence issues. The total loading time for each simulated test was adjusted to be as short as possible, but still long enough to maintain the kinetic energy as low as possible (at least equal or lower than 10% of the internal energy for most of the simulation) to ensure quasi-static loading conditions. Similarly, mass scaling was used to have a reasonable stable time increment, but without significantly affecting the kinetic energy. After several attempts, the mass was adjusted to have a stable time increment of $1 \cdot 10^{-8}$ s, while the total loading time was 0.075 s, 0.112 s, and 0.120 s for the tension, shear and combined tests, respectively. This combination was found to be the most optimum one for each particular test.

Since damage progression is quite significant before reaching final failure, element distortion becomes a classical challenge to be managed. After several trial and error explorations, the following approach was implemented. When the longitudinal damage of a volume element becomes equal to or higher than 0.999, and this element has a strain component higher than 100%, it is removed from the model. This approach guarantees that deletion is only performed when the element starts to be severely distorted, and only when it sustains no significant stiffness. Cohesive elements were not removed regardless of their damage or distortion since these were not found to lead to errors. Alternative approaches, such as using Abaqus built-in distortion control were also explored but were less efficient. However, despite of this strategy and as it will be commented later, it was impossible to simulate some of the tests entirely due to the (inevitable) distortion issues.

Several data is extracted from the simulation and compared with the experimental tests in order to validate the numerical model and demonstrate the model capabilities. The flux – strain curve is extracted from the model and compared with the experimental one. To do so, the fluxes and global strains are computed in the model in the same locations as in the experiments, following the same approach described in Section 2.1. Besides this, the crack length along the simulation is extracted and compared with the experiment. To do so, the crack length is computed simply by taking the maximum distance up to where fibre damage is equal to or larger than 0.99, see Fig. 7. Finally, the displacement fields and the failure pattern are also compared between the models and the experiments to corroborate that the displacements, deformed shape and failure pattern predicted correlate well.

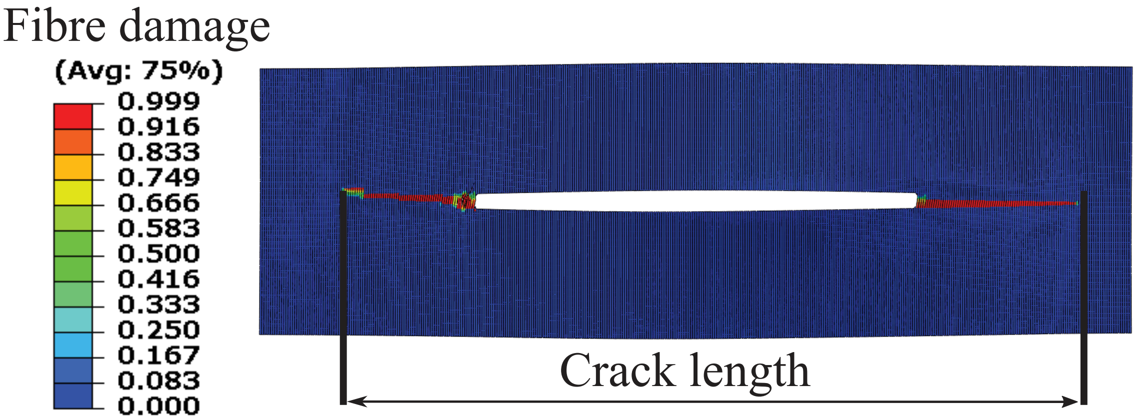

Figure 7: Methodology used to obtain the crack length in the simulations.

The models were run by using the high performance computing resources of CALMIP (Toulouse), using 72 CPUs, taking approximately 67 hours, 104 hours and 73 hours, for the tension, shear and combined cases, respectively.

3. Results and discussion

This section presents all the results from this work. First, we show a comparison between the flux - strain curve for each test. Secondly, we analyse the crack growth between the model and experiments as well as the failure mechanisms. Finally, we compare the displacements and deformed shape. Please note that some results are normalised due to confidentiality. Nonetheless, the same normalisation coefficient was used in all cases so that all results can be directly comparable.

3.1. Tension

Fig. 8 shows the longitudinal flux as a function of the longitudinal strain (plotted as continuous curves) as well as the crack length as a function of the strains (dashed curves). Notice that two experimental curves are shown to analyse the scatter.

The longitudinal flux curve of both experiment and numerical model shows a linear response until approximately a strain of 0.5%, when a plateau appears until the end of the test. Overall, the stiffness in

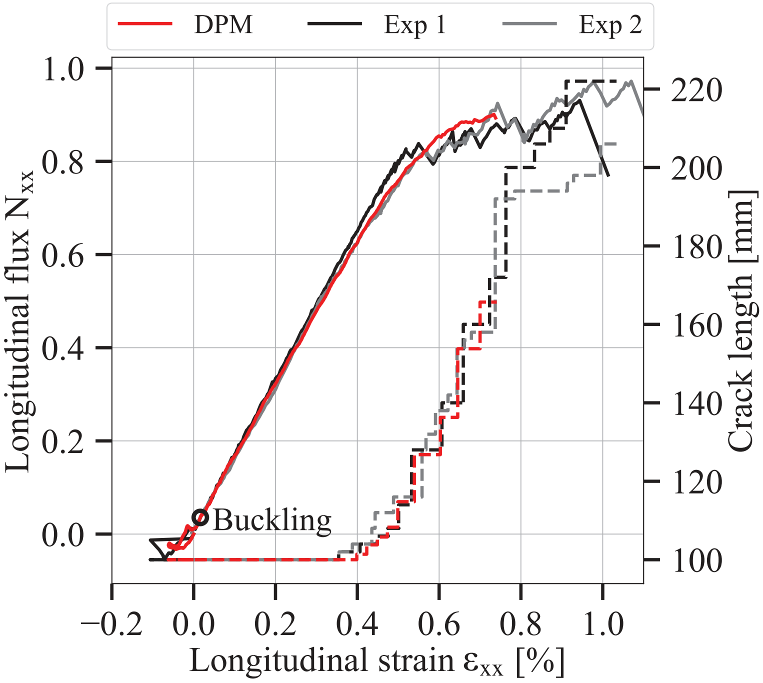

Figure 8: Tension specimen longitudinal flux – strain and crack length – strain predicted by the DPM and compared with the experimental measurements. The right Y axis indicates the crack length, while the left axis indicates the flux. Dashed curves correspond to the crack length, and continuous curves to the flux. The flux is normalised by the maximum experimental value of all tested specimens.

tension is well captured by the DPM compared with the experiments. However, the non-linear behaviour starts slightly before in the DPM, although the difference is not significant. While the experimental curves reach a strain of about 1% (when the tests were stopped), the numerical one only reaches a strain of about 0.7%. It is worth clarifying that final failure in the model does not occur at this point. Instead, the model stopped due to excessive distortion, and consequently it was not possible to simulate further from that. Modelling beyond this point is quite challenging, not only because of (inevitable) distortion issues, but also because at that point the region with damage is very extent, as will be analysed later. To simulate farther from this point, a bigger DPM region needs to be created, which would largely increase the computational time. In any case, to that extent, the agreement between model and experiments is remarkable, with the DPM capturing quite well the plateau and stiffness during the non-linear region. It should be noted that the curves do not start at zero strain and flux, this is caused by the pretension of the specimen into the VERTEX test rig. This pretension is also reasonably captured by the DPM. It is worth noting that the progressive failure of the specimen is mainly related to the thermoplastic matrix employed. Similar tests carried out in thermoset matrices presented more brittle failures [10]. In addition, buckling occurred very early in the test (around 0.02% of applied strain, see black circle in Fig. 8), as will be further analysed later.

Regarding the crack length, the model is again in excellent agreement with the experiments. Crack propagation starts at a strain of 0.4%. Soon after, when the crack length reaches a value of 110 mm (i.e., the crack has grown about 5 mm in each side), the presence of the crack starts to be noticeable in the macroscopic response, and thus, the non-linear behaviour starts. While this comparison shows that the crack growth is well captured, it gives no indication about the shape of the crack or the failure pattern, and whether the DPM is capturing it or not. For this reason, Fig. 9 presents a comparison of the failure pattern between the model and the specimen ‘exp 1’, highlighting also the crack shape, when the model stopped (i.e., around a strain of 0.7%). To ease the validation and better show the failure pattern, in the model all elements with damage equal to or larger than 0.99 are removed. Please notice that we included a picture taken by the DIC cameras and a photo from the infrared one. Overall, the failure pattern from the model resembles very well the experiments: the model captures the same 45° matrix cracks expanding from the initial notch as in the experiments (Fig. 9a and b). Further to this, the model shows that fibre damage in the central 0° ply expanded parallel to the initial notch, see Fig. 9c, which makes sense considering the tensile loading conditions. Delamination between the 0°/90° interface follows a similar pattern (Fig. 9d). Notice that notch propagation in the model is limited by the dimensions of the DPM (region 1 in Fig. 5).

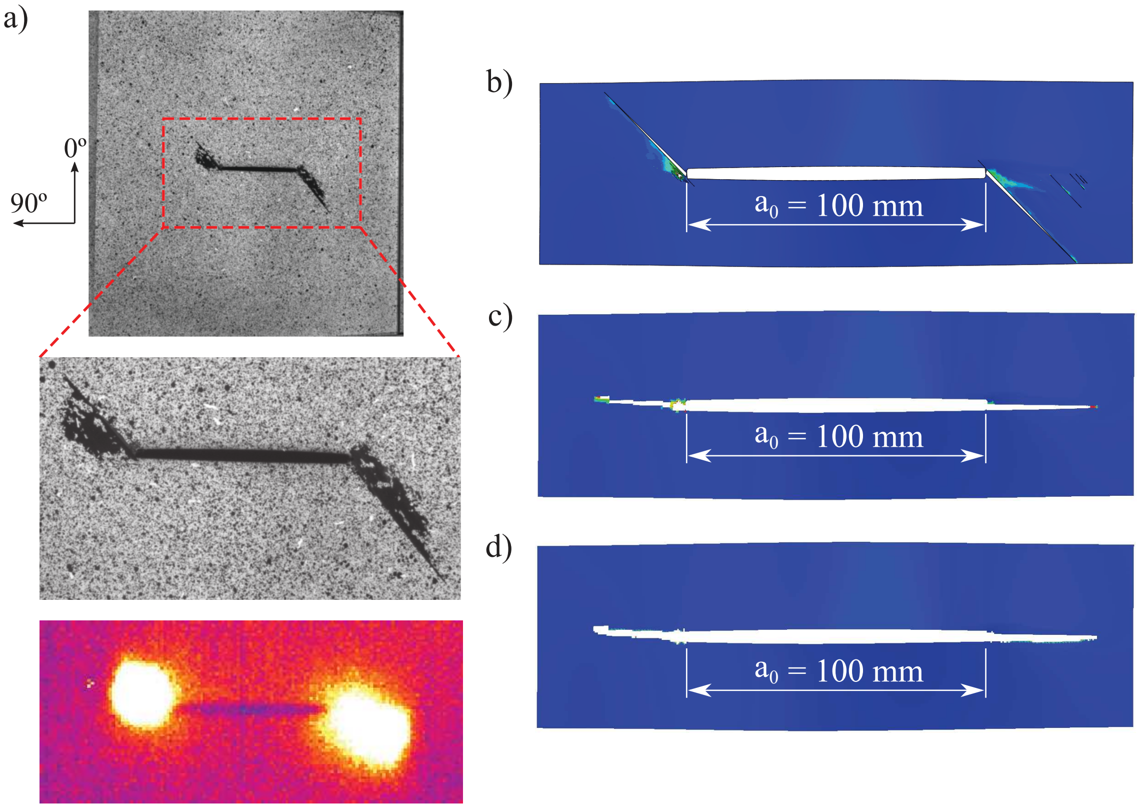

Figure 9: Tension specimen ‘exp 1’ failure pattern comparison with the DPM: a) experimental pictures, b) DPM 45° outside ply matrix cracking, c) DPM central 0° ply fibre breakage and d) DPM 0°/90° interface delamination.

The failure pattern along the simulation predicted by the numerical model is further illustrated in Fig. 10. Similarly to the observations in Serra *et al.* [33], the 0° fibre fracture and 0°/90° interface delamination propagated parallel to the notch (perpendicular to the loading direction) and did so progressively. Matrix cracking in the 90° ply also propagated continuously mainly parallel to the notch, although damage was less straight, following a kind of ‘butterfly wings’ type evolution [33], thus, being quite different to the damage seen in the outer 45° ply.

The out-of-plane displacement of the simulations was also compared with the DIC of specimen ‘exp

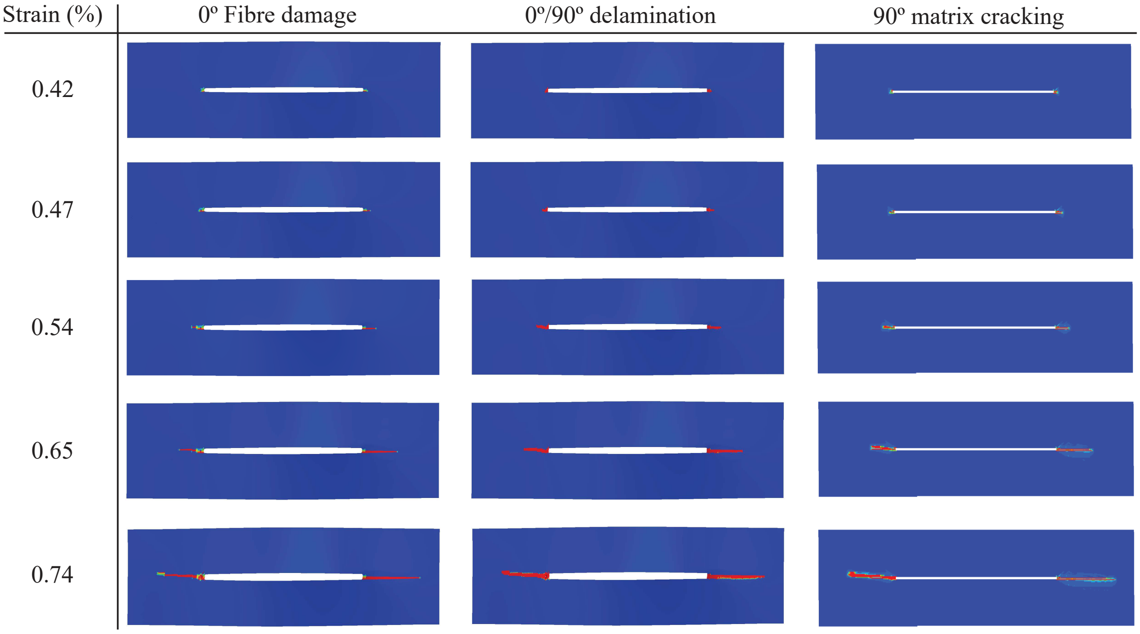

Figure 10: Numerical failure pattern predicted for the tensile specimen. Longitudinal damage is shown for the central 0º ply, delamination between the 0º/90º interface and matrix cracking for the 90º ply.

1', in order to validate the deformed shape and the application of the boundary conditions representing the VERTEX rig. Fig. 11 shows this comparison at the start of the test (preload), towards the middle (strain of 0.35%) and when the simulation was stopped (0.74% of strain). Results show the presence of buckling before starting the test, leading to a large displacement (about 7 mm) next to the notch. This is caused by the pretension of the specimen to the test rig, which constrains the specimen causing it to buckle before any jack related loading is applied [10]. Surprisingly, buckling occurred again very early after starting to load the specimen (around 0.02% of applied strain, see Fig. 8), as can be seen with the other two displacement plots at 0.35% and 0.74% of longitudinal strain (Fig. 11). This tension buckling occurs because the flanks of the central test rig box bend towards the centre, generating transverse compression, which leads to buckling of the specimen. Consequently, this tension test is in reality a biaxial longitudinal tension plus transverse compression test, although the longitudinal contribution is the main one [10].

The numerical model captures well the out-of-plane displacement (and thus the deformed shape), at the beginning and through the full test. There are small differences in the absolute values between both cases, but this mainly occurs in the edges, where the DIC fails to work correctly. As a consequence, the DPM captured well the physics of the full tension test, including the post-buckling behaviour.

3.2. Shear

Fig. 12 illustrates the shear flux as a function of the shear strain, the longitudinal flux as a function of the longitudinal strain (both plotted as continuous curves), and the crack length as a function of the shear strain (dashed curves). Although the test is meant to be pure shear, there is actually some tension loading during the test, which is the reason why the two curves are illustrated [3, 46]. This additional tension is

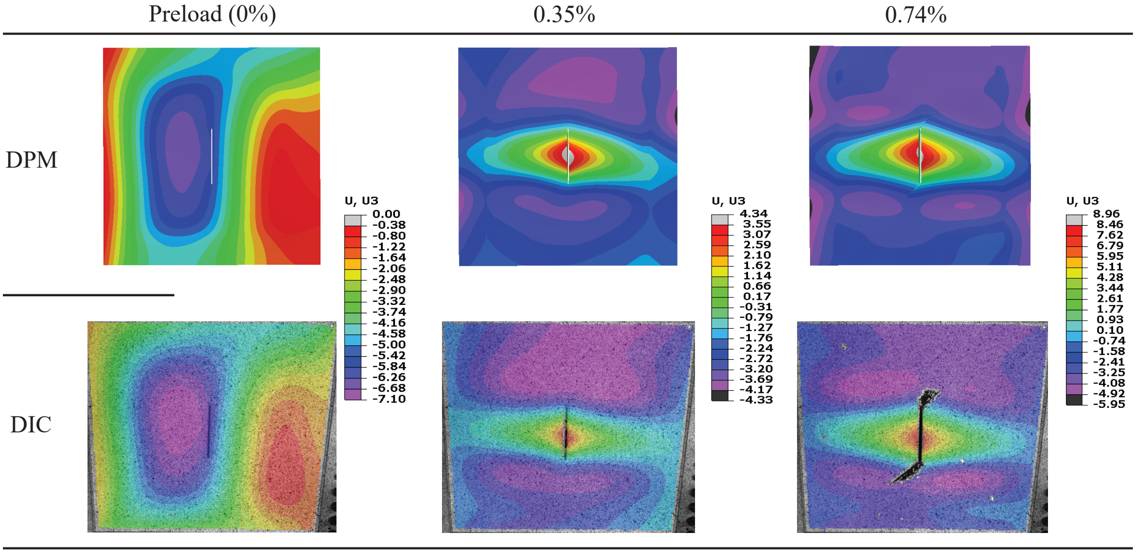

Figure 11: Comparison of the out-of-plane displacement (in mm) between the tensile specimen ‘exp 1’ and the numerical prediction at three different instants through the test (longitudinal strain indicated).

linked to the principle of post-buckling in shear. The saturation of compression stress due to shear creates an induced tension stress, which is usually referred to as the ‘diagonal tension’ theory [47–50].

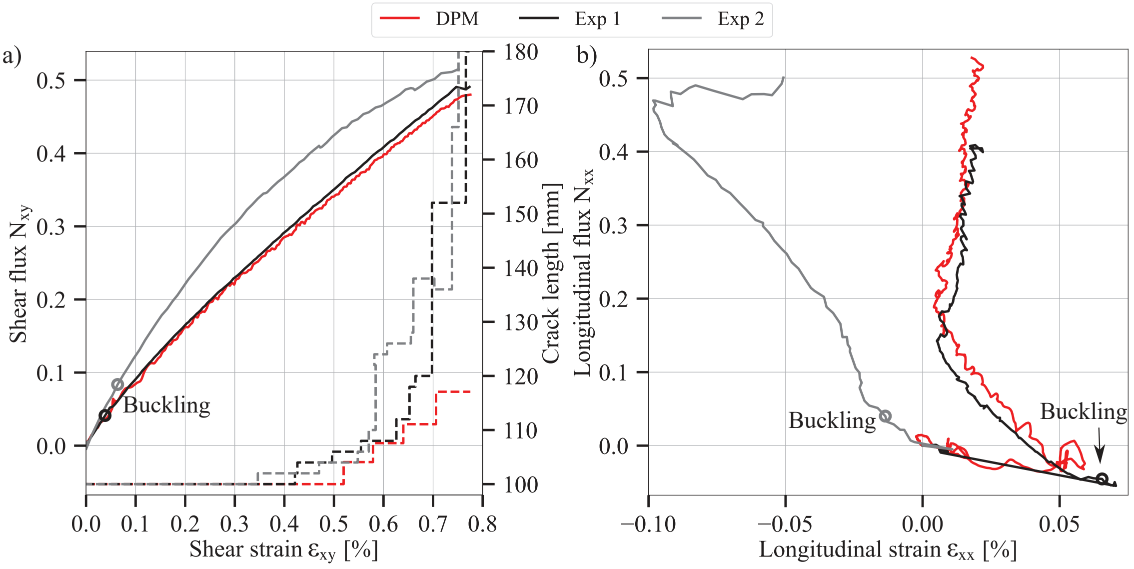

Figure 12: Shear specimen DPM predictions compared with the experimental data. a) shear flux and crack length as a function of the shear strain, and b) longitudinal flux – strain curve. The right Y axis indicates the crack length, while the left axis indicates the flux. Dashed curves correspond to the crack length, and continuous curves to the flux. The fluxes are normalised by the maximum experimental value of all tested specimens.

The DPM captures quite well both the shear flux and longitudinal flux curves (especially the shear one), following the same stiffness and behaviour. There is better agreement with ‘exp 1’ than ‘exp 2’, which can be attributed to the fact that the boundary conditions applied into the model to perform the simulation were taken from this specimen. The shear response is very non-linear, especially for ‘exp 2’. Although an initial stiffness can be identified, a non-linear response becomes clear very early in the test (around a 0.05% of shear strain). This response is attributed to the apparition of buckling, as indicated by the grey and black circles. Essentially, buckling happened after the preload, before any jack related loading was applied, as it occurred with the tension specimens. However, another buckling mode was again triggered around 0.05% of shear strain, i.e., nearly at the beginning of the test, especially, specimen 'exp 1' buckled almost immediately after loading. This buckle can be more easily identified with the longitudinal flux - strain curve response. Initially, the longitudinal flux is negative and keeps increasing until a strain of 0.07% for 'exp 1' or a strain of 0.01% for 'exp 2'. After these points, a snap-through characteristic behaviour can be identified, attributed to buckling (particularly with 'exp 1'). The DPM captures very well the buckling point, especially compared with 'exp 1' and all the post-buckling behaviour.

The results of this paper, with the presence of early buckling and an important post-buckling are quite uncommon. As a difference from classical coupon or biaxial tests, the specimens tested here are more representative of the loadings of larger structures, such as a fuselage in service. Therefore, this is one of the main highlights of this study. Despite of the complexities involved, the model is again able to capture reasonably well the physics of the problem.

Crack propagation starts slightly later in the DPM (shear strain of 0.5%, compared with a shear strain of 0.35 - 0.42% in the tests). However, the crack growth is in reasonable agreement with the two experimental measurements along the test, especially taking into account the inherent variability. The final value is, however, quite underestimated by the DPM when the test was stopped. Notice that when the crack starts to propagate no clear effect is observed on the stiffness of the specimen, contrary to what was seen under tension (see Section 3.1), without any plateau. The experimental test was stopped due to the fact that failure occurred at the corner of the specimen where it was clamped with the test bench, instead of failing at the notch. Although this crack developing at the corner did not merge with the central notch, it was decided to stop the test since this was not the desired failure mode. For this reason, no load drops are seen in the flux - strain curves. In this case, we note that we were able to model the full test.

As stated earlier, although the test is meant to be pure shear, there is actually some tension loading during the test. To better highlight this coupling, Fig. 13 presents the shear flux as a function of the longitudinal flux. Before buckling, the shear loading gives approximately pure shear (this is especially the case for 'exp 2', and in the DPM that is a more ideal case). Nonetheless, after buckling, additional loading imposes about the same amount of both shear and tensile fluxes. Again, this is related to the 'diagonal tension' theory [47–50]. This coupling is also well captured by the model. More insight on this tension-shear coupling of the VERTEX test rig can be found in [46].

Fig. 14 shows the failure pattern at the end of the test predicted by the model and compared with the specimen 'exp 1'. Like in the tensile case, the failure pattern given by the model resembles reasonably well the experimental observations. In both cases, we can notice that the crack extended mostly in a diagonal way, with a slight angle, see Fig. 14a and b. The crack length is small, especially when compared with the one seen in tension. Fibre damage mainly appeared in the -45° plies (Fig. 14c), being nearly inexistent

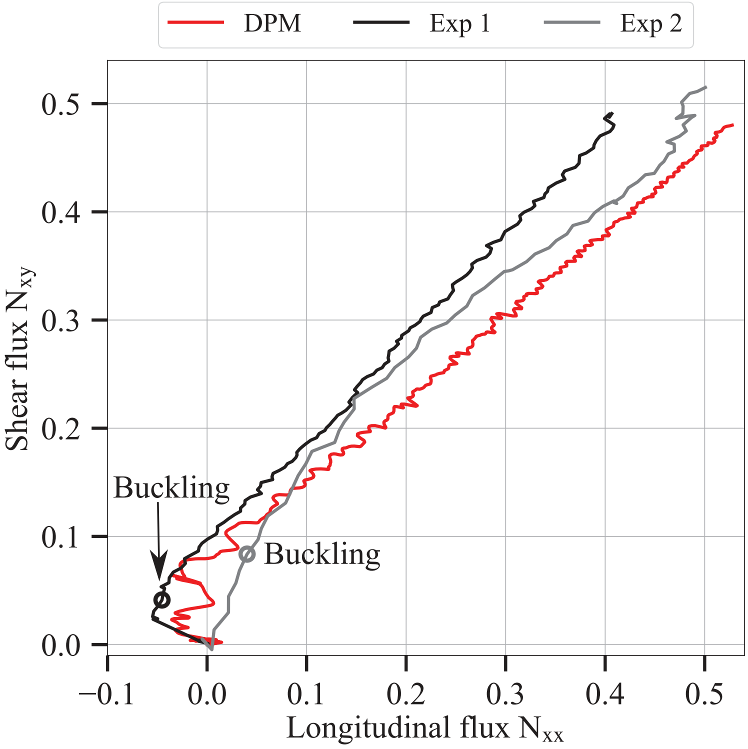

Figure 13: Shear flux as a function of the longitudinal flux for the shear test. The fluxes are normalised by the maximum experimental value of all tested specimens.

in the other plies when the simulation was stopped. Delamination between the 0º/90º interface (Fig. 14d) shows a different pattern compared to what was seen before in tension: damage extended both outwards and inwards from the crack, clearly caused by the shear loading.

The failure pattern through the simulation is more extensively detailed in Fig. 15. Fibre damage and matrix cracking are shown for the -45º ply, since this was the ply that had larger longitudinal and transverse damage though the simulation. In both cases, damage slowly grows from the notch with a 45º angle, quite differently to what was observed with the tension case in Section 3.1. On the other hand, the 0°/90° interface delamination propagates inwards and outwards of the notch as indicated before, and this progression was very continuous. Overall, the failure mechanisms and crack propagation are more complex than for the tension case as expected.

Fig. 16 presents the out-of-plane displacement of the simulations compared with the DIC of specimen ‘exp 1’ at three different instants through the tests (after preloading the specimen, towards the middle and at the end). As commented with the tensile specimen in Section 3.1, results show buckling right after performing the pretension [10]. In fact, after preloading, the deformed shape and the displacement magnitudes are in-line to the ones seen with the tensile case, which shows good repeatability. As commented before, just after starting the loading, the specimen buckled again, as shown for the other two test instants. The DPM correlates well with the experiments through the entire test, although the maximum values are slightly larger for the numerical model, just like it occurred for the tensile case. In any case, the field distribution and deformed shape is in remarkable agreement again.

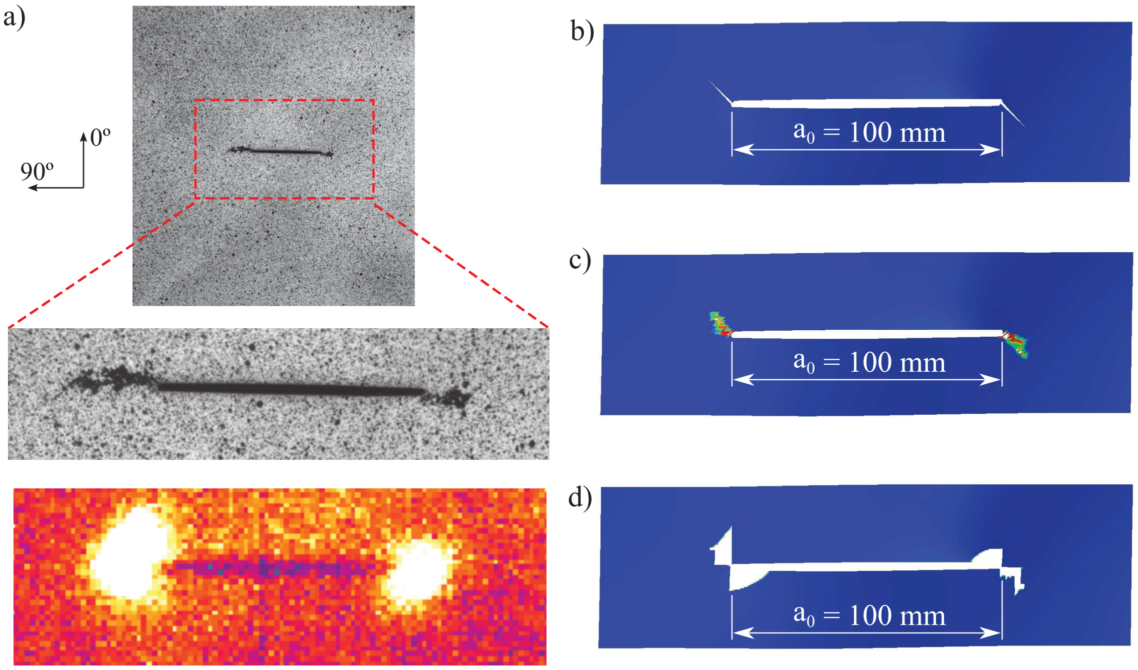

Figure 14: Shear specimen ‘exp 1’ failure pattern comparison with the DPM: a) experimental pictures, b) DPM 45° outside ply matrix cracking, c) DPM -45º ply fibre breakage and d) DPM 0°/90° interface delamination. In the model all elements with damage equal to or larger than 0.99 are removed.

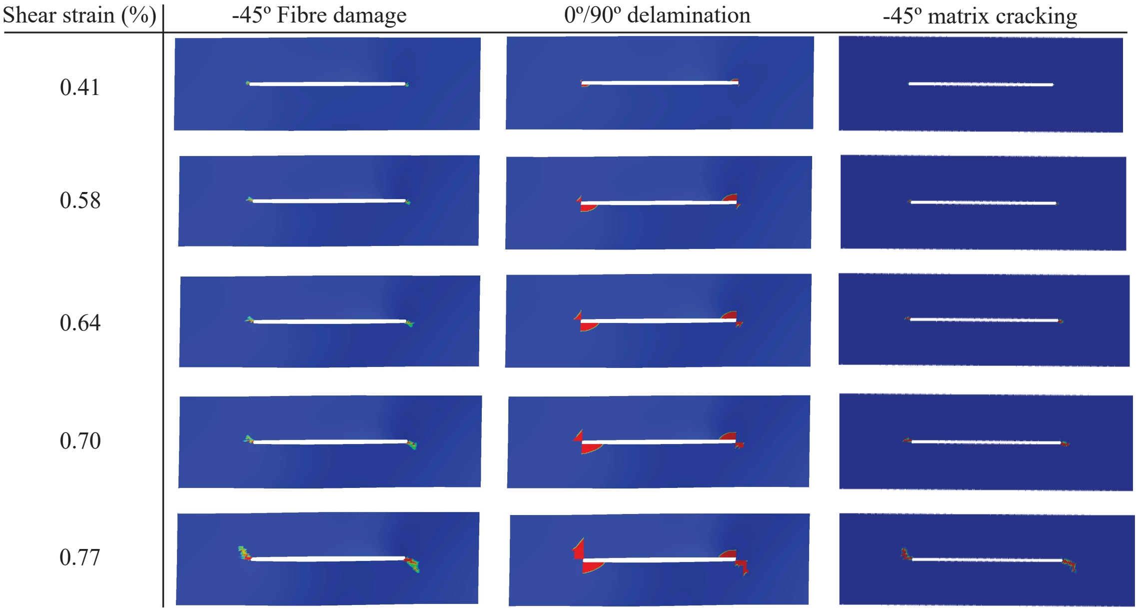

Figure 15: Numerical failure pattern predicted for the shear specimen. Longitudinal damage is shown for the -45 ply, delamination between the 0º/90º interface and matrix cracking for the -45 ply.

3.3. Combined tension and shear

Fig. 17 shows the longitudinal flux as a function of the longitudinal strain, the shear flux as a function of the shear strain (both plotted as continuous curves), and the crack length as a function of the corresponding strain (dashed curves). Notice that two experimental specimens are presented as in previous tests.

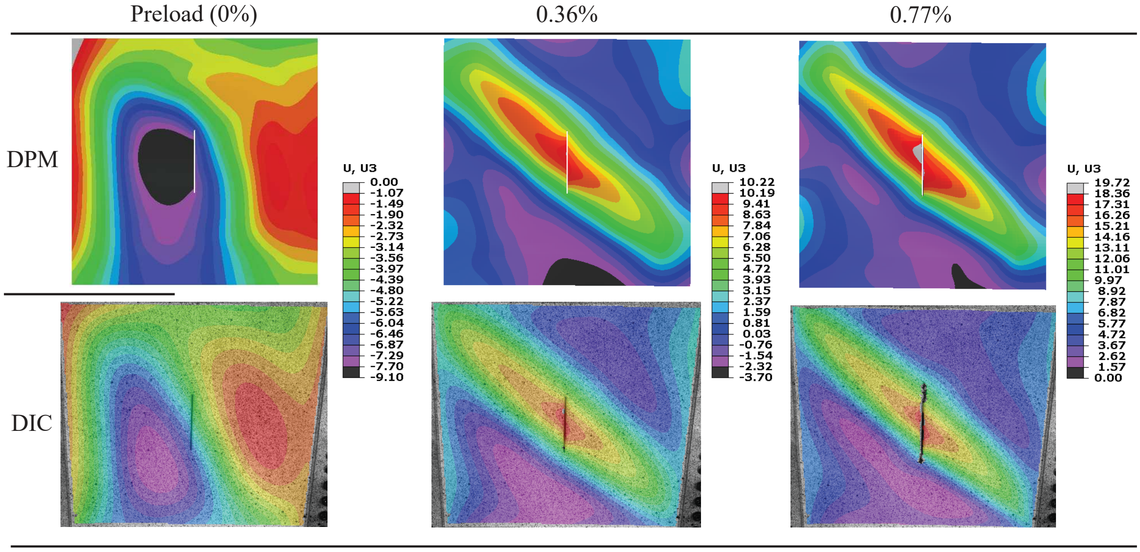

Figure 16: Comparison of the out-of-plane displacement (in mm) between the shear specimen ‘exp 1’ and the numerical prediction at three different instants through the test (shear strain indicated).

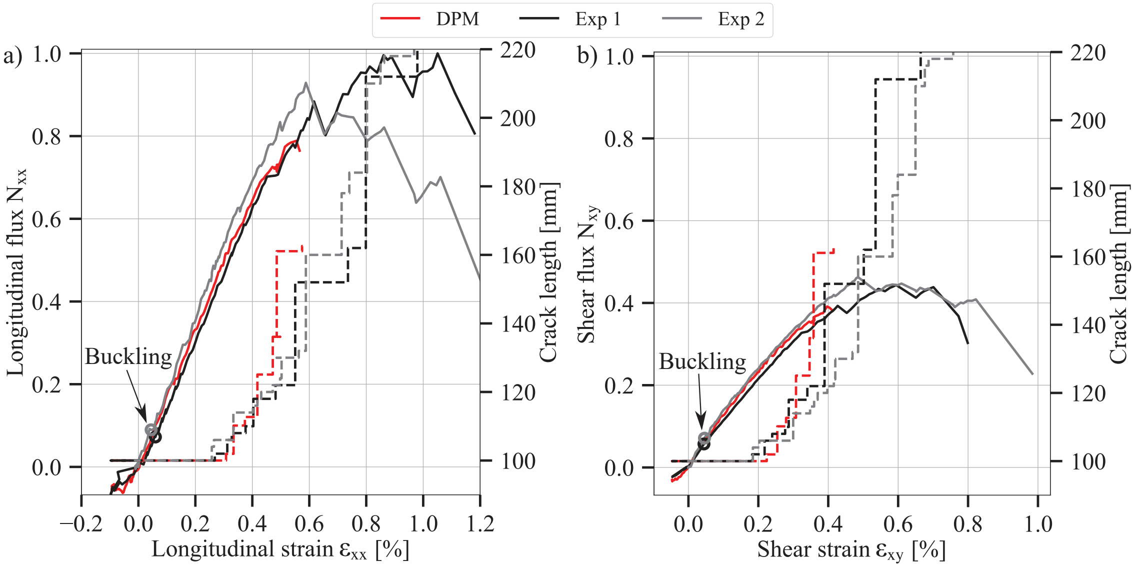

Figure 17: Combined shear and tension specimen DPM predictions compared with the experimental data. a) Longitudinal flux and crack length as a function of the longitudinal strain, and b) shear flux and crack length as a function of the shear strain. The right Y axis indicates the crack length, while the left axis indicates the flux. Dashed curves correspond to the crack length, and continuous curves to the flux. The fluxes are normalised by the maximum experimental value of all tested specimens.

Overall, the shear and longitudinal curves present a similar behaviour. Firstly, negative strains and fluxes are obtained, which are caused by the preload. After that, the behaviour is mostly linear until significant non-linearities become evident at about a longitudinal strain of 0.3% (or a shear strain of about 0.35%). For larger strains a plateau follows up, with some load drops, very similar to the behaviour encountered with the pure tensile specimen. Although it is hard to identify in the fluxes, buckling also occurred similarly to the shear specimen. First, buckling happened again after preloading the sample. After, a second buckling mode was again triggered early in the test, when the longitudinal strain was around 0.05% (or a shear strain of about 0.04%), see the circular points in Fig. 17. The DPM captures reasonably well the experimental behaviour both in tension and shear. However, the numerical model stopped at a longitudinal strain of 0.58% due to distortion issues, and it was impossible to model what happens afterwards. Hence, the authors were unable to simulate beyond that point and check whether the full experimental curve was reproducible. Nonetheless, the behaviour up to the simulated point is in reasonable agreement with the experiments.

Crack propagation starts at about the same strain for the numerical model and the two experimental coupons (0.3% and 0.2% for tensile and shear strain, respectively). The crack keeps growing linearly until a longitudinal strain of about 0.3% and a shear strain of 0.35% - 0.5%, when a large increase suddenly occurs. This response is very well predicted by the DPM. After this, the model stopped and we could not model any further. However, to this point the crack length is already 160 mm, which means that a large crack propagation has been simulated with accuracy, even the experimental magnitude is the same at this instant of the test. As explained in Section 3.1, modelling further from this point is very challenging since it requires detecting and removing distorted elements before they lead to instabilities and increasing even more the DPM size (region 1 in Fig. 5), which would lead to unfeasible computational times (the CPU time for this model was already 73 hours with 72 cpus). In line with the shear and tension specimens, when the crack starts propagating no substantial effect is seen in the flux curves. Load drops become clearly visible when the crack length is already about 130 mm, and no load drops occur until the crack is more than 160 mm. Again, this is well captured by the DPM. This behaviour highlights well that this thermoplastic material is very damage tolerant, even under complex loading.

Overall, both the longitudinal and shear strains have similar magnitudes, which confirms that the test is a combination of both loading types as desired. To better observe this, Fig. 18 shows the shear flux as a function of the longitudinal flux, for the present combined case and also for the shear and tension specimens for direct comparison. As it can be seen, there is about twice longitudinal flux than shear flux in the combined case (Fig. 18c), which indicates that the VERTEX bench imposes more tension than shear loading. Comparing all cases, the shear test (Fig. 18b) is the one that shows more shear flux, which corresponds with the desired loading conditions. On the other hand, the tension test (Fig. 18a) shows nearly no shear flux compared with the other 2 cases, which again agrees well with the desired loading of that test. Next we analyse the failure pattern of the combined specimen.

Fig. 19 illustrates the failure pattern when the simulation was stopped (i.e. at a longitudinal strain of 0.58%) compared with specimen 'exp 1'. In-line with the other tests, the failure pattern predicted correlates well with the experiments, and in general, it is quite similar to the one seen in the tension test (see Fig. 9). The damage in the outer ply shows that the crack expanded following a 45º angle, see Fig. 19a and b. Again, at this analysed point, the crack length is quite large (160 mm), and thus, much larger than for the shear case, and more in-line with the crack length seen in the tensile case. In addition, fibre damage in the 0º and -45º plies grew mostly parallel to the notch, but with a slight angle, thus, being a combination of the damage pattern seen for the 'pure' loading cases. Finally, the delamination in the 0º/90º interface (Fig. 19e) shows a crack parallel from the notch with a slight angle, nearly identical to the tension case (and very

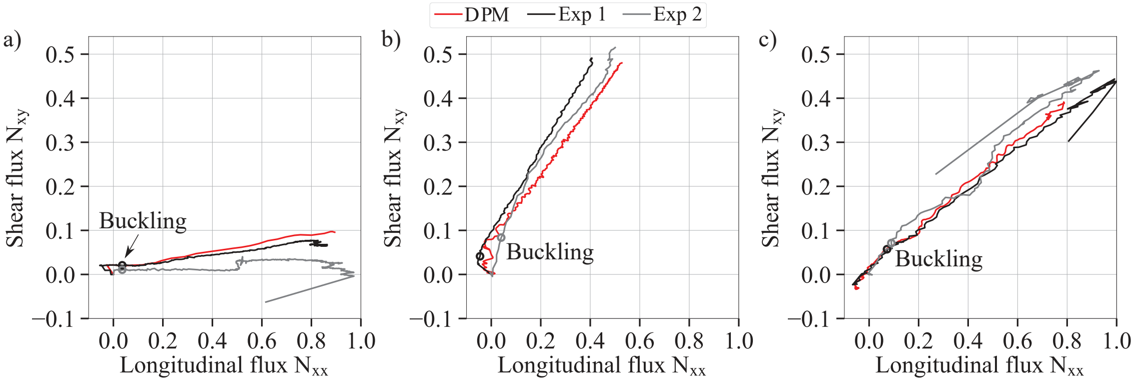

Figure 18: Shear flux as a function of the longitudinal flux. a) For the tension specimen, b) for the shear case and c) for the combined test. The fluxes are normalised by the maximum experimental value of all tested specimens.

different from the shear one). Taking into account that the failure pattern of this combined specimen seems to be more similar to the tension than to the shear one, this is consistent with the fact that this specimen is subjected to a larger amount of tensile strain than shear strain (Fig. 18).

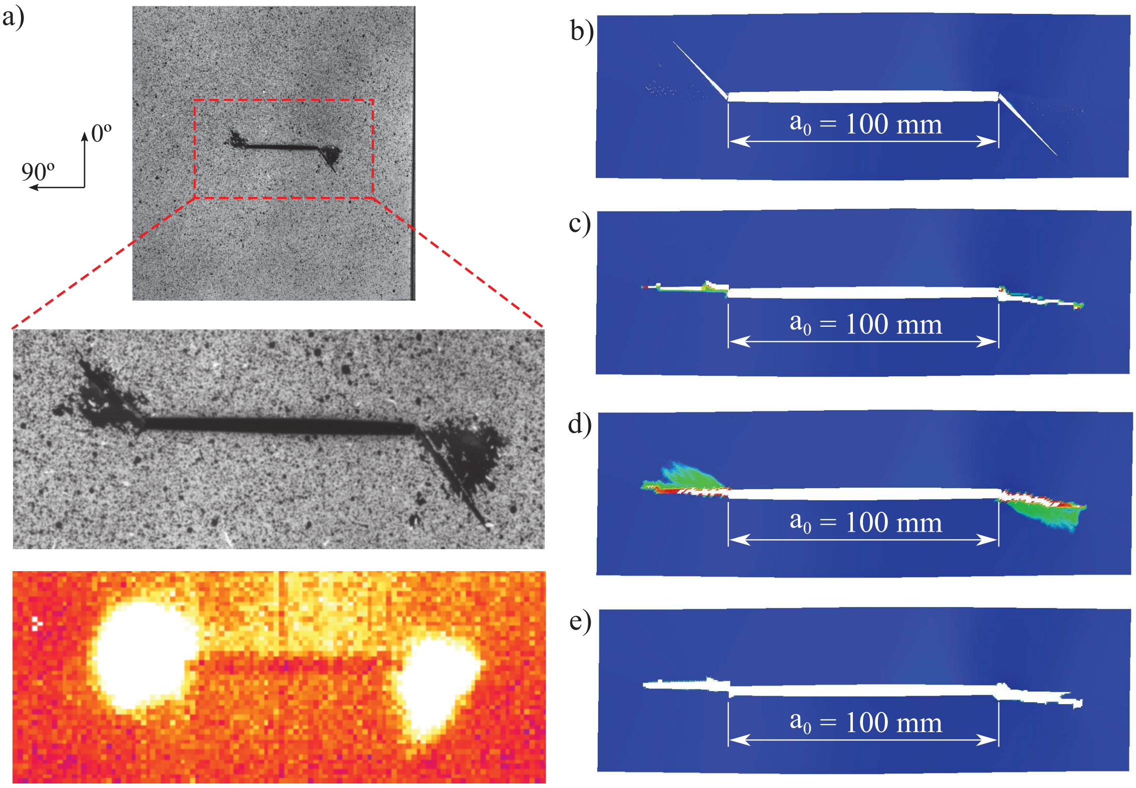

Figure 19: Combined shear and tension specimen 'exp 1' failure pattern comparison with DPM: a) experimental picture, b) DPM 45° outside ply matrix cracking, c) DPM 0º central ply fibre breakage, d) DPM -45º ply fibre breakage and e) DPM 0°/90° interface delamination. In the model all elements with damage equal to or larger than 0.99 are removed.

Next, we present the progression of the damage predicted by the model, in the same plies that were analysed for the tension and shear specimens. Fig. 20 presents the fibre breakage failure progression in the -45º and 0º plies as well as the 0º/90º interface delamination, whereas Fig. 21 shows the progression of matrix cracking in the -45º and 90º plies. The fibre damage in the -45º and 0º plies is very similar, growing slowly and smoothly from the notch with a slight angle. Both look reasonably similar to the shear and tension specimens, highlighting well the combination of both loading conditions. Likewise, the 0º/90º interface delamination grows progressively with a slight angle from the notch, as it occurred with the tension specimen (Fig. 10), but differently to what was observed with the shear case (Fig. 15). In line with this, matrix cracking in the -45º and 90º plies looks very similar, growing progressively from the notch with a slight angle, looking nearly identical to the observations from the tensile specimen (Fig. 10).

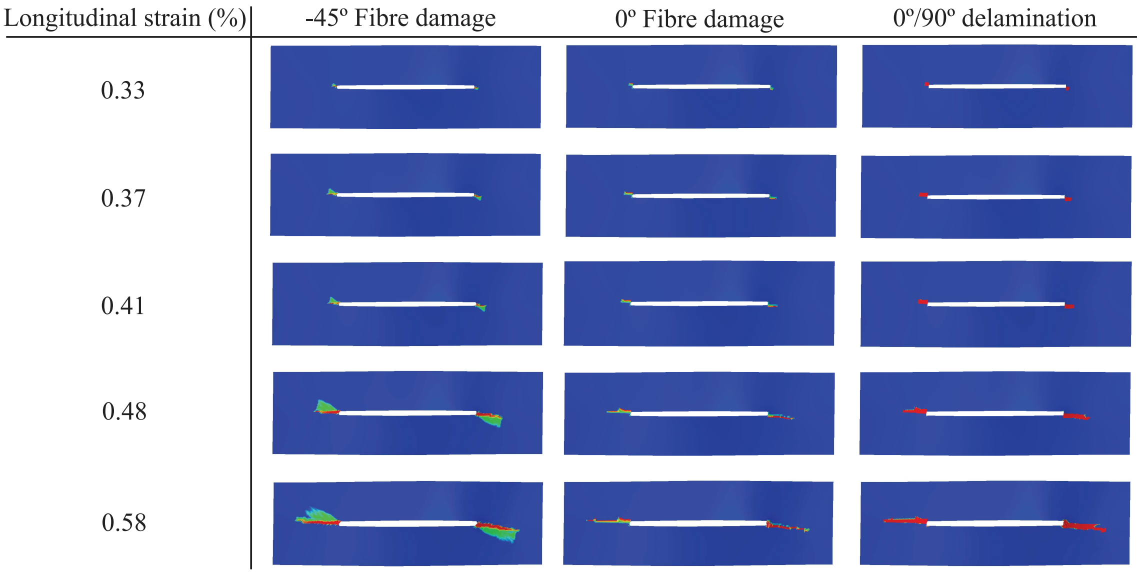

Figure 20: Fibre damage in the -45º ply, 0º ply, and delamination between the 0º/90º interface predicted for the combined loading specimen.

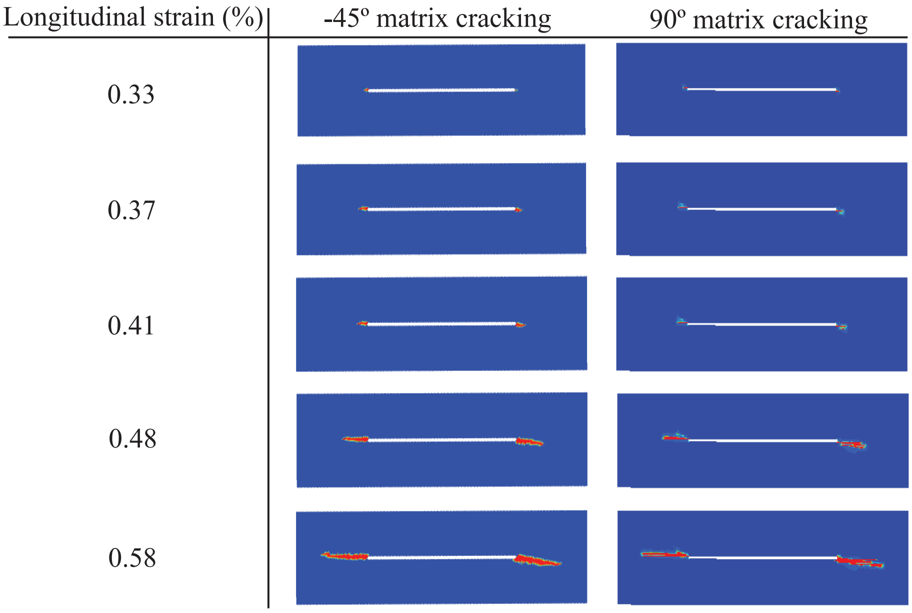

Figure 21: Matrix cracking in the -45º and 90º plies predicted for the combined loading specimen.

Fig. 22 shows a comparison between the out-of-plane displacement predicted by the DPM compared with the experimental DIC measurements of specimen ‘exp 1’ at three different instants through the tests (after preloading the specimen, towards the middle and at the end). Like the previous tension and shear specimens (Sections 3.1 and 3.2), buckling developed after preloading, which is again well captured by the DPM. Early after the test starts and some loading is applied, a second buckling mode arises, leading with the shape shown with a strain of 0.29% and 0.58%. The shape of the buckle is somewhere in-between the one observed for the tension and shear specimens (see Figs. 11 and 16). The numerical results correlate well with the experimental measurements, in terms of deformed shape and magnitude, capturing well the early buckling and post-buckling behaviour. Again, we note that there are some differences in the maximum values, but in general the agreement is remarkable.

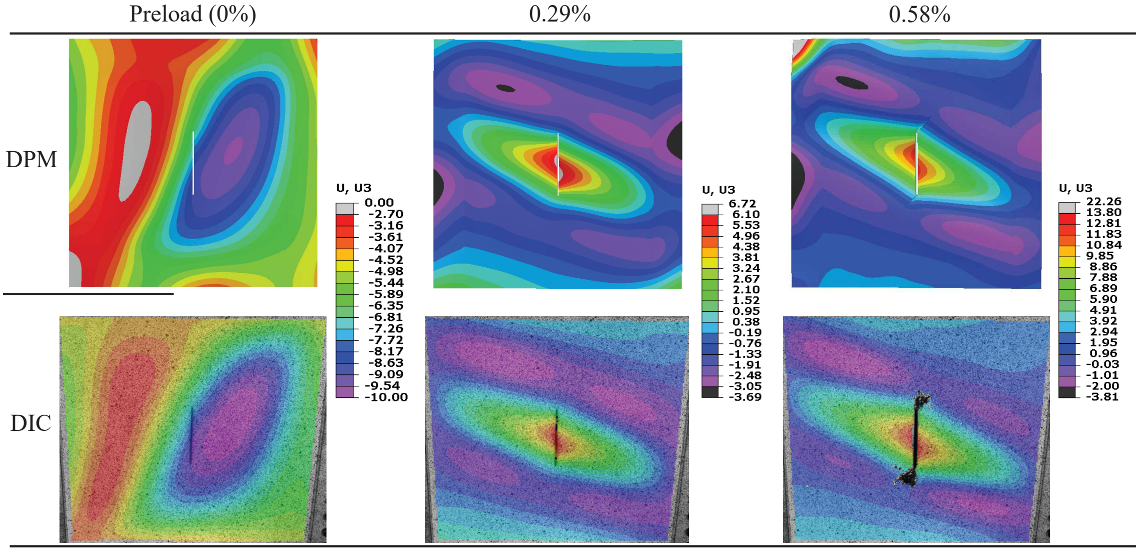

Figure 22: Comparison of the out-of-plane displacement (in mm) between the combined specimen ‘exp 1’ and the numerical prediction at three different instants through the test (longitudinal strain indicated).

To sum up the comparison between the numerical predictions of the three specimens compared with the experiments, we highlight that the model is in good agreement with the experiments in many areas. Firstly, the flux - strain response is very well captured, even the significant non-linearities and buckling found in the tests are well predicted. Secondly, crack propagation prediction presents an excellent agreement between the model and experiments, not only in magnitude, but also in terms of crack shape. Finally, the comparison with DIC highlights two things. On the one hand, it validates the methodology used to extrapolate the loading conditions from the VERTEX test rig to the model and, on the other hand, it also highlights the capabilities of the DPM to capture correctly the deformed shape, despite of the complexities near the notch.

While numerical models reproducing experimental data with accuracy are very common, for instance [8, 12, 19–21, 25], this paper goes one step beyond in the literature. Models are commonly validated and proven against experiments performed in small specimens under uniaxial loading. Nonetheless, in this work we modelled intermediate-scale specimens (400×400 mm^2) with a 100 mm notch, which are uncommon in the literature, since very few test rigs are capable of testing such specimens. In addition, we tested and modelled specimens under different loading conditions: tension, shear and a combination of both. Again, while simulations on notched, open-hole or filled-hole specimens under uniaxial tension or compression are very common [7, 8, 33], to the authors' best knowledge, there is a lack of numerical validations performed on specimens under multiaxial loading as carried out in this paper. Moreover, the tests performed in this work presented the presence of early buckling (particularly for shear, and for combined tension plus shear loading) and the development of an important post-buckling behaviour for most of the test. Again, this is quite uncommon in the literature, and the numerical results presented were able to capture this buckling. Further to this, DIC and infrared measurements were employed to corroborate the predictions of the crack propagation and failure pattern. Results demonstrate that virtual testing can also be used accurately at higher levels of the pyramid under complex loading to decrease the amount of experimental tests needed to certify composite structures. The DPM has been proven to be a robust approach to predict failure of composites at the intermediate-scale and under complex loading.

4. Conclusions

In this paper, a finite element model was developed to reproduce experimental tests on large notched carbon fibre reinforced thermoplastic laminates under tension, shear and combined loading. The numerical model makes use of the Discrete Ply Model (DPM) approach, which is able to capture fibre breakage, matrix cracking and delamination by means of combining 3D volume elements and cohesive interfaces. The fluxes as a function of the strain, the crack propagation, the failure pattern, and the predicted displacements and deformed shape were compared with the experimental data.

The results obtained show that the DPM is capable of predicting accurately the flux-strain curves of the tested notched panels for all loading conditions, even under multiaxial (tension plus shear) loading. Likewise, the crack length along the test predicted by the model correlated well against the experimental measurements obtained by infrared cameras. In addition, the crack shape and failure pattern was also reasonably captured by the model. The DPM was also able to predict accurately the displacements and deformed shape during the test, even near to the notch, as well as the buckling modes. Results from this work demonstrate the capabilities of advanced numerical models, such as the DPM, to predict accurately the response and failure of not only small coupons under uniaxial loading, but also intermediate-scale specimens (more representative of real aeronautical components) under multiaxial loading.

Future work will explore the development of more complex models including the VERTEX test rig in the model, which could allow to perform even more realistic simulations, and reduce the need to perform experimental tests. In addition, other multiaxial tests could be explored, for instance, including internal pressure and non-proportional loadings, since these may have an important effect on the buckling mode and on the crack propagation.

CRediT authorship contribution statement

José M. Guerrero: Conceptualization, Methodology, Validation, Formal analysis, Investigation, Writing - original draft, Writing - review & editing. **Christophe Bouvet:** Conceptualization, Methodology, Validation, Formal analysis, Investigation, Writing - review & editing, Supervision. **John-Eric Dufour:** Conceptualization, Methodology, Validation, Formal analysis, Investigation, Writing - review & editing, Supervision. **Joël Serra:** Conceptualization, Methodology, Validation, Formal analysis, Investigation, Writing - review & editing, Supervision.

Declaration of competing interest

The authors declare that they have no known competing financial interests or personal relationships that could have appeared to influence the work reported in this paper.

Data availability

The raw/processed data required to reproduce these findings cannot be shared at this time due to legal and/or ethical reasons.

Acknowledgements

The work conducted in this research was funded by the ‘Fondation Jean-Jacques et Felicia Lopez-Loreta pour l’Excellence Académique’ as part of the VIRTUOSE (VIRTual testing of aerOnautical StructurEs) project (https://websites.isae-supaero.fr/virtuose/). The academic authors gratefully acknowledge Airbus contribution. José M. Guerrero would also like to acknowledge the funding of the post-doc grant Margarita Salas with reference REQ2021_A_15, financed by the Spanish ‘Ministerio de Universidades’ and the European Union - Next GenerationEU. The authors would like to duly thank CALMIP High Performance Computing platform (https://www.calmip.univ-toulouse.fr) for providing the computational means required to conduct the numerical simulations under the project reference p1026.

References

[1] A. Turon, J. Costa, P. Maimí, D. Trias, J. Mayugo, A progressive damage model for unidirectional fibre-reinforced composites based on fibre fragmentation. Part I: Formulation, Composites Science and Technology 65 (13) (2005) 2039–2048. `doi:10.1016/j.compscitech.2005.04.012`.

[2] E. V. González, P. Maimí, P. P. Camanho, A. Turon, J. A. Mayugo, Simulation of drop-weight impact and compression after impact tests on composite laminates, Composite Structures 94 (11) (2012) 3364–3378. `doi:10.1016/j.compstruct.2012.05.015`.

[3] J. Serra, J. E. Pierré, J. C. Passieux, J. N. Périé, C. Bouvet, B. Castanié, Validation and modeling of aeronautical composite structures subjected to combined loadings: The VERTEX project. Part 1: Experimental setup, FE-DIC instrumentation and procedures, Composite Structures 179 (2017) 224–244. `doi:10.1016/j.compstruct.2017.07.080`.

[4] Chapter 8 - building block approach, in: B. Backman (Ed.), Composite Structures, Design, Safety and Innovation, Elsevier, Oxford, 2005, pp. 99–110. `doi:https://doi.org/10.1016/B978-008044545-8/50008-5`.

[5] O. Vallmajó, I. R. Cózar, C. Furtado, R. Tavares, A. Arteiro, A. Turon, P. P. Camanho, Virtual calculation of the B-value allowables of notched composite laminates, Composite Structures 212 (December 2018) (2019) 11–21. `doi:10.1016/j.compstruct.2018.12.049`.

[6] J. Serra, J. E. Pierré, J. C. Passieux, J. N. Périé, C. Bouvet, B. Castanié, C. Petiot, Validation and modeling of aeronautical composite structures subjected to combined loadings: The VERTEX project. Part 2: Load envelopes for the assessment of panels with large notches, Composite Structures 180 (2017) 550–567. `doi:10.1016/j.compstruct.2017.08.055`.

[7] I. R. Cózar, J. M. Guerrero, P. Maimí, A. Arteiro, S. García-Rodríguez, M. Herman, A. Turon, Influence of unidirectional composite failure envelope shape on predicting compressive failure of a laminate with a filled-hole, Composites Part B 276 (November 2023) (2024) 111352. `doi:10.1016/j.compositesb.2024.111352`.

[8] C. Furtado, G. Catalanotti, A. Arteiro, P. J. Gray, B. L. Wardle, P. P. Camanho, Simulation of failure in laminated polymer composites: Building-block validation, Composite Structures 226 (June) (2019) 111168. `doi:10.1016/j.compstruct.2019.111168`.

[9] C. Furtado, L. F. Pereira, R. P. Tavares, M. Salgado, F. Otero, G. Catalanotti, A. Arteiro, M. A. Bessa, P. P. Camanho, A methodology to generate design allowables of composite laminates using machine learning, International Journal of Solids and Structures 233 (October 2020) (2021) 111095. `doi:10.1016/j.ijsolstr.2021.111095`.

[10] F. Grotto, C. Bouvet, B. Castanié, J. Serra, Experimental behaviour of aeronautical notched carbon fibre reinforced thermoplastic panels under combined tension-shear-pressure loadings, Engineering Failure Analysis 146 (January) (2023). `doi:10.1016/j.engfailanal.2023.107075`.

[11] S. R. Hallett, B. G. Green, W. G. Jiang, M. R. Wisnom, An experimental and numerical investigation into the damage mechanisms in notched composites, Composites Part A: Applied Science and Manufacturing 40 (5) (2009) 613–624. `doi:10.1016/j.compositesa.2009.02.021`.

[12] J. Serra, C. Bouvet, B. Castanié, C. Petiot, Scaling effect in notched composites: The Discrete Ply Model approach, Composite Structures 148 (2016) 127–143. `doi:10.1016/j.compstruct.2016.03.062`.

[13] B. Y. Chen, T. E. Tay, P. M. Baiz, S. T. Pinho, Numerical analysis of size effects on open-hole tensile composite laminates, Composites Part A: Applied Science and Manufacturing 47 (1) (2013) 52–62. `doi:10.1016/j.compositesa.2012.12.001`.

[14] A. B. De Morais, Open-hole tensile strength of quasi-isotropic laminates, Composites Science and Technology 60 (10) (2000) 1997–2004. `doi:10.1016/S0266-3538(00)00089-0`.

[15] G. Zucco, V. Oliveri, M. Rouhi, R. Telford, G. Clancy, C. McHale, R. O'Higgins, T. Young, P. Weaver, D. Peeters, Static test of a variable stiffness thermoplastic composite wingbox under shear, bending and torsion, The Aeronautical Journal 124 (1275) (2020) 635–666. `doi:10.1017/aer.2019.161`.

[16] R. Peters, Buckling tests of flat rectangular plates under combined shear and longitudinal compression (1946).
URL https://ntrs.nasa.gov/api/citations/19930082377/downloads/19930082377.pdf

[17] J. M. Whitney, R. J. Nuismer, Stress Fracture Criteria for Laminated Composites Containing Stress Concentrations, Journal of Composite Materials 8 (3) (1974) 253–265. `doi:10.1177/002199837400800303`.

[18] P. P. Camanho, G. H. Erçin, G. Catalanotti, S. Mahdi, P. Linde, A finite fracture mechanics model for the prediction of the open-hole strength of composite laminates, Composites Part A: Applied Science and Manufacturing 43 (8) (2012) 1219–1225. `doi:10.1016/j.compositesa.2012.03.004`.

[19] P. Maimí, P. Camanho, J. Mayugo, C. G. Dávila, A continuum damage model for composite laminates: Part I - Constitutive model, Mechanics of Materials 39 (10) (2007) 897–908. `doi:10.1016/j.mechmat.2007.03.005`.

[20] P. Maimí, P. P. Camanho, J. A. Mayugo, C. G. Dávila, A continuum damage model for composite laminates: Part II - Computational implementation and validation, Mechanics of Materials 39 (10) (2007) 909–919. `doi:10.1016/j.mechmat.2007.03.006`.

[21] P. P. Camanho, M. A. Bessa, G. Catalanotti, M. Vogler, R. Rolfes, Modeling the inelastic deformation and fracture of polymer composites-Part II: Smeared crack model, Mechanics of Materials 59 (2013) 36–49. `doi:10.1016/j.mechmat.2012.12.001`.

[22] F. Laurin, N. Carrere, C. Huchette, J. F. Maire, A multiscale hybrid approach for damage and final failure predictions of composite structures, Journal of Composite Materials 47 (20-21) (2013) 2713–2747. `doi:10.1177/0021998312470151`.

[23] A. Quintanas-corominas, P. Maimí, E. Casoni, A. Turon, J. A. Mayugo, G. Guillamet, M. Vázquez, A 3D transversally isotropic constitutive model for advanced composites implemented in a high performance computing code, European Journal of Mechanics / A Solids 71 (May 2017) (2018) 278–291. `doi:10.1016/j.euromechsol.2018.03.021`.

[24] I. Cózar, F. Otero, P. Maimí, E. González, S. Miot, A. Turon, P. Camanho, A three-dimensional plastic-damage model for polymer composite materials, Composites Part A: Applied Science and Manufacturing 163 (September) (2022) 107198. `doi:10.1016/j.compositesa.2022.107198`.

[25] I. R. Cózar, F. Otero, P. Maimí, E. V. González, A. Turon, P. P. Camanho, An enhanced constitutive model to predict plastic deformation and multiple failure mechanisms in fibre-reinforced polymer composite materials, Composite Structures 330 (December 2023) (2024) 117696. `doi:10.1016/j.compstruct.2023.117696`.

[26] R. P. Tavares, A. R. Melro, M. A. Bessa, A. Turon, W. K. Liu, P. P. Camanho, Mechanics of hybrid polymer composites: analytical and computational study, Computational Mechanics 57 (3) (2016) 405–421. `doi:10.1007/s00466-015-1252-0`.

[27] R. P. Tavares, F. Otero, J. Baiges, A. Turon, P. P. Camanho, A dynamic spring element model for the prediction of longitudinal failure of polymer composites, Computational Materials Science 160 (October 2018) (2019) 42–52. `doi:10.1016/J.COMMATSCI.2018.12.048`.

[28] J. M. Guerrero, J. A. Mayugo, J. Costa, A. Turon, A 3D Progressive Failure Model for predicting pseudo-ductility in hybrid unidirectional composite materials under fibre tensile loading, Composites Part A: Applied Science and Manufacturing 107 (February) (2018) 579–591. `doi:10.1016/j.compositesa.2018.02.005`.

[29] C. Breite, A. Melnikov, A. Turon, A. B. de Morais, C. Le Bourlot, E. Maire, E. Schöberl, F. Otero, F. Mesquita, I. Sinclair, J. Costa, J. A. Mayugo, J. M. Guerrero, L. Gorbatikh, L. N. McCartney, M. Hajikazemi, M. Mehdikhani, M. N. Mavrogordato, P. P. Camanho, R. P. Tavares, S. M. Spearing, S. V. Lomov, S. Pimenta, W. V. Paepegem, Y. Swolfs, Detailed experimental validation and benchmarking of six models for longitudinal tensile failure of unidirectional composites, Composite Structures 279 (October 2021) (2022) 114828. `doi:10.1016/j.compstruct.2021.114828`.

[30] C. Bouvet, B. Castanié, M. Bizeul, J. J. Barrau, Low velocity impact modelling in laminate composite panels with discrete interface elements, International Journal of Solids and Structures 46 (14-15) (2009) 2809–2821. `doi:10.1016/j.ijsolstr.2009.03.010`.

[31] D. Scano, E. Carrera, M. Petrolo, Use of the 3D Equilibrium Equations in the Free-Edge Analyses for Laminated Structures with the Variable Kinematics Approach, Aerotecnica Missili & Spazio 103 (2) (2024) 179–195. `doi:10.1007/s42496-023-00177-2`.

[32] M. Trombini, M. Enea, M. R. Arruda, A. Pagani, M. Petrolo, E. Carrera, 1D higher-order theories for quasi-static progressive failure analysis of composites based on a full 3D Hashin orthotropic damage model, Composites Part B: Engineering 270 (May 2023) (2024) 111120. `doi:10.1016/j.compositesb.2023.111120`.

[33] J. Serra, C. Bouvet, B. Castanié, C. Petiot, Experimental and numerical analysis of Carbon Fiber Reinforced Polymer notched coupons under tensile loading, Composite Structures 181 (2017) 145–157. `doi:10.1016/j.compstruct.2017.08.090`.

[34] J. Serra, A. Trellu, C. Bouvet, S. Rivallant, B. Castanié, L. Ratsifandrihana, Combined loadings after medium velocity impact on large CFRP laminated plates: Discrete ply model simulations, Composites Part C: Open Access 6 (2021). `doi:10.1016/j.jcomc.2021.100203`.

[35] R. Rutar, J. Serra, Q. Bausiere, C. Bouvet, Experimental characterization of tensile and compressive translaminar fracture toughness coupling multi-physics measurements, Engineering Fracture Mechanics 291 (September) (2023) 109568. `doi:10.1016/j.engfracmech.2023.109568`.

[36] Dassault Systemes/ SIMULIA, ABAQUS, Inc. ABAQUS version 2018 Documentation. (2018).

[37] V. Achard, C. Bouvet, B. Castanié, C. Chirol, Discrete ply modelling of open hole tensile tests, Composite Structures 113 (1) (2014) 369–381. `doi:10.1016/j.compstruct.2014.03.031`.

[38] Z. Hashin, Failure Criteria for Unidirectional Fiber Composites, Journal of Applied Mechanics 47 (June) (1980) 329–334. `doi:10.1115/1.3153664`.

[39] I. Standard, Plastics — methods for determining the density of non-cellular plastics, (ISO 1183-1), 2019.
URL https://www.iso.org/standard/74990.html

[40] E. Standards, Aerospace series - carbon fibre reinforced plastics - unidirectional laminates - tensile test parallel to the fibre direction, (EN 2561), 1995.
URL www.en-standard.eu

[41] E. Standards, Aerospace series - carbon fibre reinforced plastics; unidirectional laminates - tensile test perpendicular to the fibre direction, (EN 2597), 1999.
URL www.en-standard.eu

[42] E. Standards, Aerospace series. carbon fibre thermosetting resin - unidirectional laminates. compression test parallel to fibre direction, (EN 2850), 2017.
URL www.en-standard.eu

[43] ISO 15024:2001. Fibre-reinforced plastic composites — Determination of mode I interlaminar fracture toughness, GIC, for unidirectionally reinforced materials, ISO (2023).
URL https://www.iso.org/standard/25581.html

[44] ASTM D7905/D7905M-19e1. Standard Test Method for Determination of the Mode II Interlaminar Fracture Toughness of Unidirectional Fiber-Reinforced Polymer Matrix Composites, ASTM International, West Conshohocken, PA (2019).
URL https://www.astm.org/d7905_d7905m-19e01.html

[45] C. Leopold, S. Harder, C. Buggisch, W. Liebig, B. Fiedler, Influence of 90°-layer thickness on damage initiation and propagation in cfrp cross-ply laminates, 2016.

[46] F. Grotto, O. Peta, C. Bouvet, B. Castanié, J. Serra, Testing Structural Elements under Multiaxial Loading: A Numerical Model of the Bench to Understand and Predict Complex Boundary Conditions, Aerospace 11 (1) (2024). `doi:10.3390/aerospace11010068`.

[47] H. Wagner, Flat sheet metal girders with very thin metal web. Part I: General theories and assumptions, NACA-TM-604 (1931).

[48] A. Murphy, M. Price, C. Lynch, A. Gibson, The computational post-buckling analysis of fuselage stiffened panels loaded in shear, Thin-Walled Structures 43 (9) (2005) 1455–1474. `doi:10.1016/j.tws.2005.03.010`.

[49] P. Kuhn, J. P. Peterson, L. R. Levin, A Summary of Diagonal Tension Part I - Methods of Analysis, NACA-TN-2661 (1952).

[50] K. P, Stresses in Aircraft and shell structures, 1st Edition, McGraw-Hill Book Co., 1956.